INL/EXT-21-64705

Advancements in modeling fuel pulverization and cladding behavior during a LOCA

September 30, 2021

Technical Report

Kyle A. Gamble[1], Larry K. Aagesen[1], Sudipta Biswas[1], Wen Jiang[1], Antonio Martin Recuero[1], Jason D. Hales[1], Daniel VanWasshenova[1], Michael W. D. Cooper[2], Nathan Capps[3], and Ryan Sweet[3]

[1]Idaho National Laboratory
[2]Los Alamos National Laboratory
[3]Oak Ridge National Laboratory

Idaho National Laboratory

INL is a U.S. Department of Energy National Laboratory
operated by Batelle Energy Alliance, LLC

Advancements in modeling fuel pulverization and cladding behavior during a LOCA

Technical Report

Kyle A. Gamble[1], Larry K. Aagesen[1], Sudipta Biswas[1], Wen Jiang[1], Antonio Martin Recuero[1], Jason D. Hales[1], Daniel VanWasshenova[1], Michael W. D. Cooper[2], Nathan Capps[3], and Ryan Sweet[3]

[1]Idaho National Laboratory
[2]Los Alamos National Laboratory
[3]Oak Ridge National Laboratory

September 30, 2021

Idaho National Laboratory
Computational Mechanics and Materials Department
Idaho Falls, Idaho 83415

http://www.inl.gov

Prepared for the
U.S. Department of Energy
Office of Nuclear Energy
Under U.S. Department of Energy-Idaho Operations Office
Contract DE-AC07-05ID14517

Page intentionally left blank

Abstract

During a loss-of-coolant accident (LOCA), it is possible for nuclear fuel rods to undergo a three-step process known as fuel fragmentation, relocation, and dispersal (FFRD). The chance of FFRD occurring increases as the fuel burnup increases. To support the nuclear industry's desire to increase the discharge burnup of nuclear fuels in light-water reactors (LWRs), it is imperative to understand the mechanisms driving the evolution of FFRD.

In this work, a multiscale modeling approach is used to garner insight into underlying mechanisms leading to the fine fragmentation (also known as pulverization) of nuclear fuel during a LOCA. This report includes a summary of the atomistic and phase-field studies to develop a new pulverization criterion for use in the engineering-scale Bison fuel performance code. Details are also provided on cladding model improvements related to hydrogen/hydride embrittlement and damage and anisotropic thermal creep. The new models are used on the existing integral and separate effects LOCA validation cases available in Bison.

Page intentionally left blank

Acknowledgments

This report was authored by a contractor of the U.S. Government under Contract DE-AC07-05ID14517. Accordingly, the U.S. Government retains a non-exclusive, royalty-free license to publish or reproduce the published form of this report, or allow others to do so, for U.S. Government purposes.

Contributions have been provided by Los Alamos National Laboratory, an affirmative action/equal opportunity employer, is operated by Triad National Security,LLC, for the National Nuclear Security Administration of the U.S. Department of Energy under Contract No. 89233218CNA000001.

Contributions have been provided by Oak Ridge National Laboratory.

This research made use of the resources of the High Performance Computing Center at Idaho National Laboratory, which is supported by the Office of Nuclear Energy of the U.S. Department of Energy and the Nuclear Science User Facilities under Contract No. DE-AC07-05ID14517.

Page intentionally left blank

Contents

List of Figures

List of Tables

Acronyms

AFC	advanced fuels campaign
EOC	end-of-cycle
EPRI	Electric Power Research Institute
FFRD	fuel fragmentation, relocation, and dispersal
FUMAC	Fuel Modelling in Accident Conditions
HBS	high-burnup structure
INL	Idaho National Laboratory
LANL	Los Alamos National Laboratory
LHR	linear heat rate
LOCA	loss-of-coolant accident
LWR	light-water reactor
MOOSE	Multiphysics Object-Oriented Simulation Environment
NEAMS	Nuclear Energy Advanced Modeling and Simulation
NRC	U.S. Nuclear Regulatory Commission
ORNL	Oak Ridge National Laboratory
PCT	peak cladding temperature
PWR	pressurized-water reactor
SATS	severe accident test station

1. Introduction

As nuclear fuel vendors and utilities submit licensing applications to extend the operational burnup of nuclear power plants for efficiency, flexible operation, and economics, the phenomenon of fuel fragmentation, relocation, and dispersal (FFRD) has been identified as priority issue. In order to improve the nuclear community's understanding of the mechanisms driving FFRD, a multi-institutional approach involving industry, universities, and national laboratories is required. This work summarizes the advancements in multiscale modeling to better understand the causes of fine fuel fragmentation during a loss-of-coolant accident (LOCA) through a multi-laboratory effort. New capabilities for modeling the behavior of the cladding during a LOCA are also provided.

The report starts with an overview of model developments at the atomistic scale, contributed by Los Alamos National Laboratory (LANL). These atomistic studies helped inform modeling parameters at the mesoscale (phase-field). The report continues with a summary of the mesoscale model development and implementation into the Bison [1] fuel performance code. Next, two new features for cladding modeling that have been added are introduced, namely hydrogen/hydride embrittlement and damage as well as a preliminary anisotropic creep model. These new models are then added to a variety of integral and separate effects validation cases from the Bison LOCA test suite to evaluate their impact on the predictions and comparisons to experiment. The report concludes with two sections contributed by Oak Ridge National Laboratory (ORNL) on applications of Bison to an industry-relevant problem as well as details on collaborative efforts between the advanced fuels campaign (AFC) and Nuclear Energy Advanced Modeling and Simulation (NEAMS) programs. A chapter detailing future areas of research is provided.

2. Atomistic Scale Calculations

High-burnup structure (HBS) morphology is typically characterized by the formation of small sub-grains and the coalescence of smaller bubbles into micron-sized bubbles. In addition, nm-sized bubbles have been observed by Sonoda et al. [2] to decorate the sub-grain boundaries. Here, we summarize work done to explore the phenomena that govern bubble over-pressurization in the cooler periphery of the pellet (where HBS forms) during steady-state operation. Then, during a subsequent temperature transient, the expansion of the over-pressurized bubbles, leading to grain boundary fracture, has been investigated.

2.1 Bubble Pressure Evolution

In Fiscal Year 2020 (FY-20), simulations were carried out to predict the impact of irradiation-enhanced U defect diffusivity on bubble pressure over a wide range of temperatures. The work leveraged the Centipede cluster dynamics code, which can capture the experimentally observed irradiation-enhanced diffusivity of Xe and U in UO_2. Critically, the code includes a variety of defects, such as U and Xe interstitials. In FY-20, molecular dynamics (MD) simulations were used to derive expressions for the reaction energies of U interstitial and vacancy defects with bubbles, as a function of the bubble pressure. These pressure-dependent reaction energies were incorporated into the Centipede code and used to predict the steady-state bubble pressure as a function of temperature. At low temperatures relevant to the HBS region, the uranium interstitials, which are highly mobile relative to vacancies, could rapidly diffuse to the bubbles. This results in the over-pressurization of bubbles to high Xe/SD ratios. Note that Xe/SD is the ratio between the number of Xe atoms in the bubble to the number of UO_2 formula units removed to make the void the Xe atoms occupy. It is, therefore somewhat analogous to the bubble pressure.

In FY-21, this work was extended by deriving bubble-pressure-dependent energies for the reaction of Xe-containing defects with bubbles. As before, this was based on the analysis of MD data for the change in the bubble energy as the numbers of Xe atoms or vacancies in a bubble are changed combined with the annihilation energy due to removing defects from the bulk lattice. Figure 2.1a shows the reaction energy of U and Xe defects with a bubble as a function of the Xe/SD ratio. It can be seen for all defects that, if Xe/SD = 0 (i.e. a void), it is always favorable to eliminate the defect from the lattice. However, as the bubble Xe/SD ratio increases, it becomes less favorable, and eventually unfavorable, to incorporate Xe or U interstitials into the bubble. This is due to the energy penalty associated with further increasing the

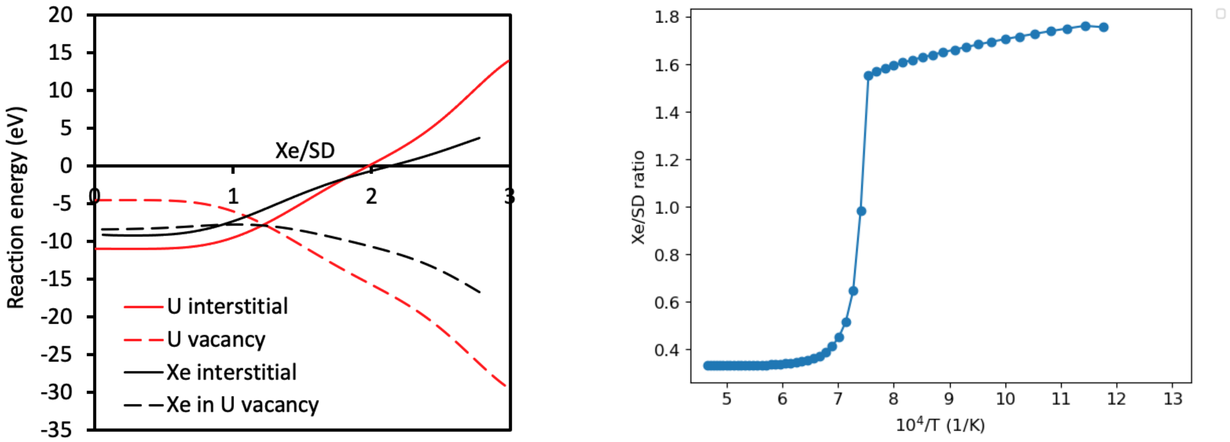

(a) (b)

Figure 2.1. a) The reaction energy for defects with a fission gas bubbles as a function of the Xe/SD ratio of the bubble for a U interstitial (red solid line), a U vacancy (red dashed line), a Xe interstitial (black solid line), and a Xe in a U vacancy (black dashed line). b) The steady-state Xe/SD ratio predicted from cluster dynamics simulations using the reactions shown in a).

bubble pressure, either by increasing the number of Xe atoms or by reducing the number of U vacancies that make up the bubble. Conversely, the reaction of U vacancies with the bubble becomes more favorable for high Xe/SD as they act to relieve the bubble pressure. The reaction of a Xe atom in a single uranium vacancy becomes less favorable as a function of Xe/SD for Xe/SD = 0 to 1, as it increases the pressure of those bubbles; however, if Xe/SD>1, the defect acts to decrease the bubble pressure and therefore the reaction becomes more favorable. Similar functions were applied to the full range of Xe-containing defects that the Centipede code solves for. Figure 2.1b shows the steady-state Xe/SD ratio as a function of inverse temperature predicted by cluster dynamics simulations using Centipede that include the pressure-dependent defect-bubble reactions shown in Figure 2.1a. A clear transition from low to high Xe/SD ratios occurs as the temperature is reduced. Importantly, for the low temperatures relevant to the periphery, where HBS forms, the Xe/SD ratio approaches 1.8, representing highly over-pressurized bubbles. This is due to the impact of highly mobile irradiation-enhanced concentrations of interstitials at low temperatures, which increase the bubble pressure, whereas at high temperatures, diffusion is dominated by vacancies, which reduce the bubbles pressure. In the next section, the impact of high-pressure bubbles on grain boundary strength during temperature transients is evaluated.

2.2 Fracture Simulations

In FY-20 and FY-21, under work initially funded by Electric Power Research Institute (EPRI) and now continuing under NEAMS, MD simulations have been carried out to investigate the impact that highly over-pressurized bubbles (such as those predicted to form in Section 2.1) have on the fracture of grain boundaries.

Under the EPRI-funded project, it was shown that, if a sufficiently high number of 2-nm bubbles with a Xe/SD ratio of 2, were located at a grain boundary, when that system was exposed to a temperature ramp to $>$ 1400 K, the bubbles could drive the boundary apart, even without any external strain applied to the supercell. Furthermore, even at lower temperatures or for fewer bubbles, there was still a significant reduction in the applied stress required to fracture the grain boundary due to the internal stresses imparted on the grain boundary by the expanding bubbles. A range of bubble sizes, pressures, and number density were evaluated in that project and the results can be found in the report by Andersson and Cooper [3]. It was suggested in that work that there was the need to increase the amount of time over which the system is equilibrated before the stress-strain analysis is conducted, as well as the need to explore Xe/SD ratios in the range of 1.0–1.5. Therefore, in FY-21, this work was continued under NEAMS with those objectives in mind. Figure 2.2a shows the supercell length in the direction perpendicular to the grain boundary during an extended equilibration simulation lasting 2 ns (as opposed to the 200 ps equilibration conducted originally). The supercell length is shown as a strain with respect to the length at 300 K, and the system contained eight 2-nm inter-granular bubbles with a Xe/SD ratio of 1.4, which had not been considered previously. Note that the strain in Figure 2.2a is not applied; rather, initially it is due to thermal expansion and then to relaxation around the inter-granular bubbles, such as microcracking. It can be clearly seen from Figure 2.2a that the extended equilibration time allows for some additional relaxation (see the jump in length at around 750 ps that is likely due to a microcracking event). Following equilibration, a strain was applied to the system in the direction normal to the grain boundary, during which the stress on the supercell in the same direction was calculated. Figure 2.2b shows the stress as a function of strain during the stress-strain analysis. It can be seen that there is a linear increase in stress at first. Once a threshold stress is reached, a fracture event causes a drop in the system strength. This is followed by a recovery in strength and a return to linear behavior. This process repeats itself until the grain faces fully separate and the stress approaches zero. The strong reduction in peak stress as a function of temperature, shown in Figure 2.2b for a Xe/SD ratio of 1.4, is also seen for the full range of Xe/SD=1.0 to 1.5. This was also predicted in the EPRI work for higher Xe/SD ratios of 1.5–2.0. The reduction is especially pronounced for higher values of Xe/SD, indicating the importance of high bubble pressures for the mechanical and fragmentation properties of HBS grain boundaries.

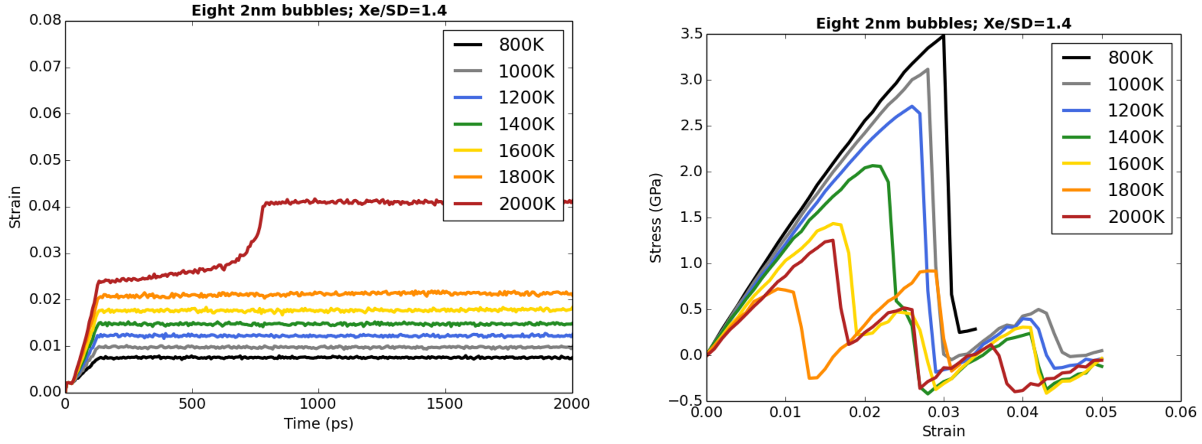

(a)

(b)

Figure 2.2. a) The length of the supercell normal to the grain boundary (shown as the strain relative to the length at 300 K) during equilibration to various temperatures at zero pressure. b) A stress-strain analysis of the system following equilibration at various temperatures.

3. Engineering-Scale Model Implementation and Testing

3.1 Mesoscale Informed Pulverization Threshold

Nuclear fuel vendors and utilities in the U.S. are currently seeking permission to operate fuel at higher burnup levels. To enable this, a major issue that must be addressed is the possibility of fine fragmentation or pulverization of fuel that can occur during the temperature transient accompanying a LOCA. Pulverization results in the formation of numerous small fragments, including a significant number of fragments of size 100 μm [4] or less. These small fragments can escape from the fuel rod in the event of an accompanying cladding breach.

To aid these efforts toward burnup extension, the capability to predict the onset of pulverization using Bison is desired. An empirical model has been implemented in Bison based on a summary of data presented in Ref. [4]. However, this model is solely a function of burnup and temperature and thus is only applicable to the conditions in which the data used to derive it were taken. To allow for greater flexibility and applicability to a wider range of operating conditions, a new model based on fuel microstructure has been developed and added to Bison in FY-21.

The causes of pulverization during LOCA transients are not fully understood, but it has been correlated with the partial or complete formation of the HBS in UO_2 fuel. Bubbles in the HBS region are believed to be overpressurized at the onset of HBS formation. As these bubbles undergo a LOCA transient, their temperatures further increase, leading to a greater pressure, and therefore greater stresses are felt in the surrounding fuel matrix. It is hypothesized that the greater pressures exerted by the bubbles on the subgrain boundaries surrounding the fuel may be the cause of pulverization.

Based on this hypothesis, criteria for pulverization based on both analytical and mesoscale simulation methodologies were developed and implemented in Bison in FY-21. Mesoscale simulations were also used to better understand the mechanisms of HBS formation and the response of bubbles during transients. Further details about this work are available in a separate milestone, Ref. [5]; a brief summary is provided here. First, a phase-field model was used to better understand the evolution of bubble pressure as a result of HBS formation and provide an initial bubble pressure for the Bison model. The simulations showed that gas atoms diffuse from grain interiors to the new grain boundaries created during HBS formation and diffuse rapidly along these grain boundaries to reach existing bubbles. This causes an increase in bubble pressure in existing bubbles, leading to bubble growth during steady-state operation. Next, to simulate the response of HBS bubbles to a LOCA transient, a phase-field model that accounts for the bubble pressure and surface tension of the bubble-matrix interface on the stress state of the surrounding fuel was used. Simulations with this model showed that bubble size did not change significantly during the duration of the transient. Finally, a phase-field fracture model was used to study fragmentation patterns in the HBS and to inform a pulverization criterion for Bison. A function for the critical pressure for pulverization to occur in a representative bubble was fit to data from the phase-field fracture simulations, and this function was implemented as a material property in Bison, `UO2PulverizationMesoscale`. For comparison, an analytical model for the critical pressure for pulverization was developed and implemented within the same material property. This material property compares the critical pressure for pulverization to occur (using either the simulation or analytical criterion) with the current gas bubble pressure, based on an initial pressure determined from the model in the first section and the current temperature. If the current gas bubble pressure is greater than the critical pressure for pulverization, pulverization is deemed to have occurred locally. Comparison of the results of these mesoscale-informed models with the existing empirical criterion are provided in Section 4.

3.2 Hydrogen/Hydride Embrittlement and Damage

Zircaloy cladding oxidizes at a slow rate under LWR conditions. Some of the free hydrogen enters the cladding, and at sufficient concentrations, hydrides form. These hydrides naturally occur as circumferential platelets with a normal to the plane of a platelet in the radial direction. At elevated temperatures and changing stress conditions, like those seen during the drying of spent fuel, the hydrogen can dissolve and platelets can reform in a radial direction with a normal in the circumferential direction. Hydrides weaken the cladding due to their brittle properties. This weakening is most important with radial hydrides since tensile hoop stresses are much larger than tensile radial stresses.

Rashid et al. [6] introduced a model for Zircaloy with hydrides intended to integrate the fracture and failure of hydrides under tension with the typical Zircaloy response. This model has been implemented in Bison based on subroutines provided to Idaho National Laboratory (INL) through a contract with Mark Rashid several years ago.

Inputs to the model include elastic and plastic material properties, the volume fraction of radial and circumferential hydrides, and a damage strain parameter for both Zircaloy and hydride.

The basic building block of the model is the arrangement described in Figure 3.1 with intact and damaged hydride platelet and matrix materials. The fraction of these materials is

$$f_p + f_m = 1 \tag{3.1}$$

$$f_1 + f_3 = f_p \tag{3.2}$$

$$f_2 + f_4 = f_m \tag{3.3}$$

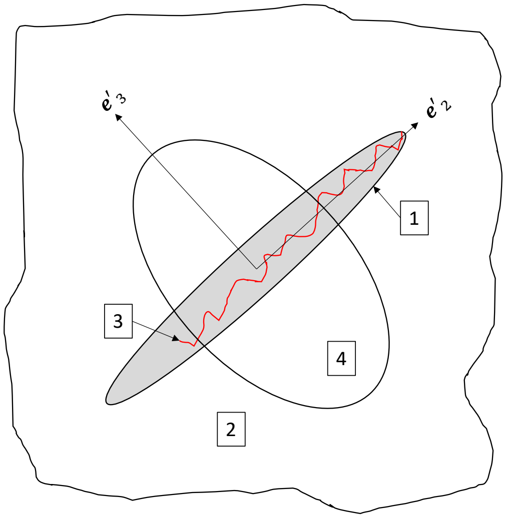

Figure 3.1. Four domains in the damage model: 1, intact platelet; 2, intact matrix; 3, damaged platelet; and 4, damaged matrix. Based on Figure 3 in [6].

where f is the fractional amount with subscripts p, m, 1, 2, 3, and 4 representing platelet, matrix, and domains 1 through 4 based on Figure 3.1. As damage develops, one or both of f_3 and f_4 are greater than zero.

The model relies on an elastic-plastic constitutive rule for both the Zircaloy and the hydride phases. Considering first the undamaged state, the two constituents are constrained to experience the same strains in the plane of the hydride and the same stresses out of the plane of the hydride. For undamaged platelet and matrix,

$$\sigma'_{zz} = f_1 \sigma'^{p}_{zz} + (1 - f_1)\sigma'^{m}_{zz} \tag{3.4}$$

where the prime indicates that the stress is oriented in the platelet's local coordinate frame.

More generally,

$$\sigma = \sum_{i=1}^{4} f_i \sigma^i. \tag{3.5}$$

The model enforces zero stress across damaged hydride and damaged Zircaloy phases. Any load perpendicular to damaged material is carried by the undamaged material.

Damage is measured by tracking the strain normal to the platelet. Increased strain increases the damage. With increasing damage, more material (hydride and Zircaloy) is considered damaged and less considered undamaged.

The damage function used in the model depends on the maximum normal strain, ϵ, the damage parameter

ϵ_0, a volume fraction, f, and a damage fraction parameter, f_0. Damage, d, is given as

$$d = \begin{cases} 0 & \text{for } \epsilon < \epsilon_0/2 \\ \left(\dfrac{\epsilon - \epsilon_0/2}{\bar{\epsilon} - \epsilon_0/2}\right)^2 & \text{for } \epsilon_0/2 < \epsilon < \bar{\epsilon} \\ 1 & \text{for } \epsilon > \bar{\epsilon} \end{cases} \tag{3.6}$$

where

$$\bar{\epsilon} = \epsilon_0(1 - f_0 + f_0/f). \tag{3.7}$$

When the volume fraction, f, is one, $\bar{\epsilon} = \epsilon_0$ with damage beginning at $\epsilon_0/2$ and ending at ϵ_0 through a quadratic transition. With a smaller, more typical volume fraction, damage begins at the same point but reaches one at a larger strain.

Overall damage in the matrix is computed as the sum of the damage in the hydride squared and a separate damage calculation for the matrix. In this way, matrix damage is often lower than the hydride damage but reaches one when the hydride is fully damaged.

By considering radial hydrides alongside a matrix composed of Zircaloy with circumferential hydrides and also circumferential hydrides alongside a matrix composed of Zircaloy with radial hydrides, the interaction between all three is determined.

In this model, damage is driven purely by tensile strains in the radial and circumferential directions. With no tensile strain in these directions, no damage will be computed.

3.2.1 Demonstration Problems

The cladding damage model involves two sets of hydrides with independent orientations and a plasticity model operating on the hydrides and the Zircaloy material. The model computes a consistent tangent matrix along with the stress, and this requires numerous transformations between coordinate frames.

To show that the basic behavior of the model was correct, we ran a pair of elementary tests. The first is the so-called patch test [7] in which a 3D cube is meshed as seven elements with one element at the center of the cube and one face of each of the remaining six elements at one of the faces of the cube. The interior element is warped such that each element has a unique geometry. By applying particular normal and shear strains through displacements at the eight nodes, the cube experiences three sets of normal stresses and three sets of shear stresses. The cladding damage model correctly computed the six stresses for the patch test. A corresponding test was run for axisymmetric elements (those used for typical 2D fuel pin calculations), and the results were as expected.

Next, we performed a rotation test. In this test, loads are applied and maintained through prescribed displacements at the nodes of a cube. The cube is loaded in one axial direction. Then, the cube is rotated, maintaining the axial load, through 90 degrees. At this point, the stress has been transformed from, say, the x direction to the y direction. For the cladding damage model, which contains normal directions as part of its formulation, the transformation of normals must occur also. The cladding damage model correctly

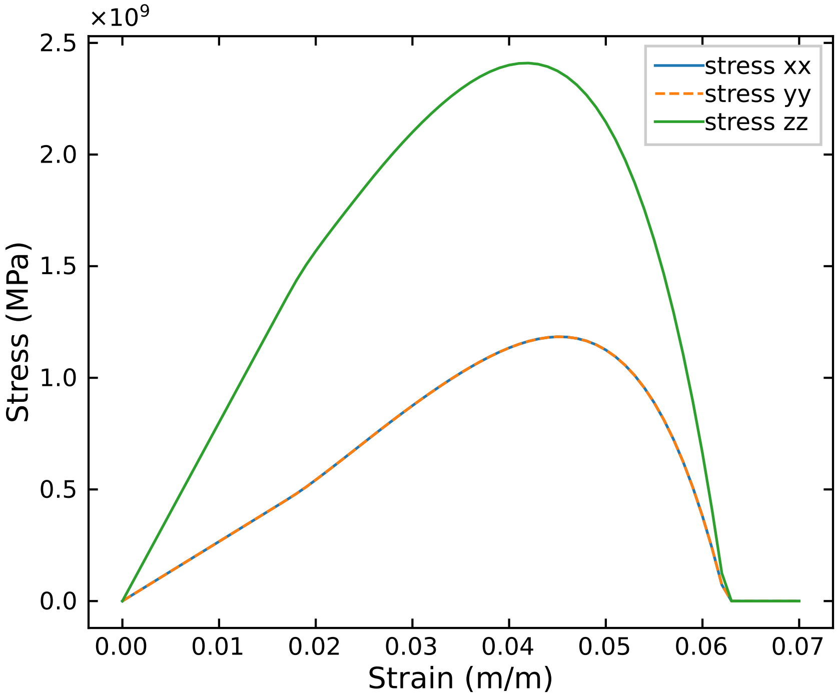

Figure 3.2. Evolution of stress for an element fixed except for a tensile displacement in the z direction. Cracking (damage) is first seen at a strain of about 0.02. When fully damaged, the stress returns to zero.

computes the stress rotation and the rotation of the internal normals.

In both of the tests just described, damage was not active. To test damage, we used a single cubic element. The radial hydrides had a normal in the z direction, and the circumferential hydrides had a normal in the x direction. The displacements in the x and y directions were fixed, as were the displacements in the z direction on the back of the element. The front (positive z face) of the element was pulled in tension.

Tensile stresses build in the z direction with increasing strain. Due to the Poisson effect, tensile stresses also build in the x and y directions. At a certain point, damage begins to occur, with the result that the slope of the stress/strain curve begins to decrease. With continually increasing strain in the z direction, the stresses reach a maximum and then decrease to zero. The stress/strain evolution can be seen in Figure 3.2.

In a second, similar demonstration, an additional shear load was introduced by displacing the front face in the y direction at one-tenth the rate of the axial displacement. The resulting stress behavior is similar to the preceding case, with stresses returning to zero based on increasing damage. See Figure 3.3.

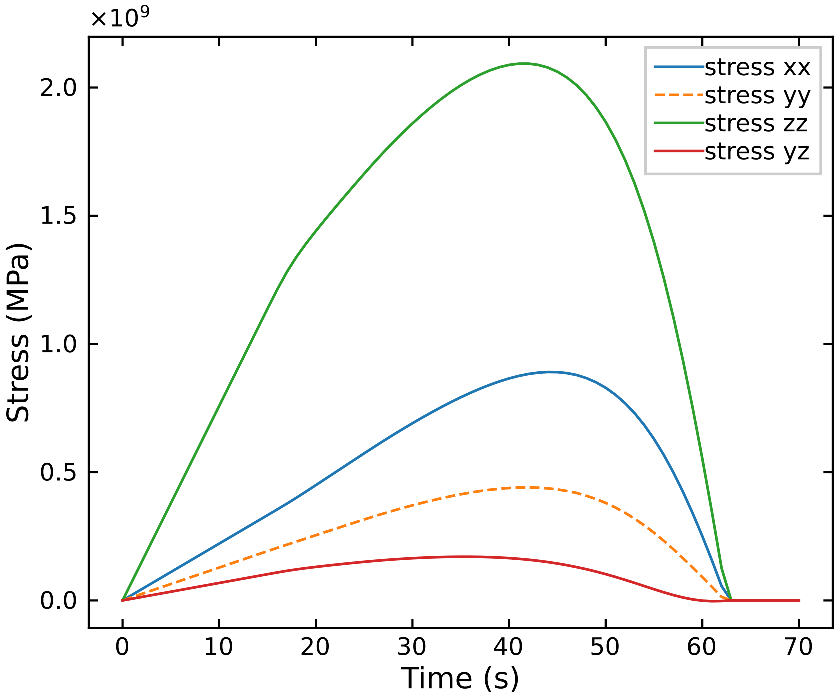

Figure 3.3. Evolution of stress for an element fixed except for a tensile displacement in the z direction and a vertical displacement on the same face. When fully damaged, the stress returns to zero.

3.2.2 Example of Burst Behavior

Figures 6 and 7 in [6] show experimental data and model predictions for “two axial tensile tests.” The figures give inner, mid-wall, and outer cladding stresses as functions of strain and also show a single experimental data curve in each figure. The three model predictions in each figure have the same general character, namely an elastic response, a plastic response, and a return to zero stress (due to damage). The paper gives some detail about the test but not enough detail to recreate the calculation. Among the missing information is the amount of radial hydrides in the tubes.

As these are tensile tests, with no mention of other constraints or pressure loads, one would expect the dominant strain to be in the axial direction and to be positive. Since hydrides do not form with normals in the axial direction, their effect in that direction is minor. More importantly in this case, the axial strain is positive, leading to small negative strains in the other two directions. Since the radial and hoop strains are negative, the model is not expected to produce damage in those directions. Still, the figures in [6] indicate that damage has been modeled. Explanations for this situation include setting up the model in an atypical fashion or modeling a tube that was loaded with internal pressure rather than with an axial load.

Despite the paper not providing a complete set of input data for those problems, we chose to model a tube according to the information available while filling in unknowns using engineering judgement. The result is a model of a slice of irradiated Zircaloy cladding with 20 elements through the cladding wall. The material contains 524 ppm hydrogen and is at 25°C. The results are in Figure 3.4 where the stress is shown at the inner wall, mid-wall, and outer wall locations. The results are qualitatively similar to those shown in [6]. The outer wall reaches a higher stress but is fully damaged at the lowest strain, with the inner wall seeing the lowest stress and full damage at the highest strain. This follows expectations given that the model assumes a greater concentration of hydrides at the outer surface than the inner surface of the cladding.

3.2.3 Rodlet Burst

The cladding damage model was applied to a short rodlet under a pressure load. Model parameters are listed in Table 3.1. The model was restrained at the bottom edge from vertical motion, and the pressure was applied to the interior of the tube. The pressure was increased until significant stress, strain, and damage developed, at which point the simulation could proceed no further.

Figure 3.5 shows volume fractions of initial radial hydrides, initial circumferential hydrides, final intact radial hydrides, and final intact matrix. Greatest damage is seen at the inner surface of the rodlet.

Table 3.1. Analysis parameters for rodlet under pressure.

Inner radius, r_i (m)	0.004125
Outer radius, r_o (m)	0.004535
Height, h (m)	0.1
Radial hydride fraction (-)	$0.005 * (1 + \exp(-(y - (h/2)^2)/(2(h/10)^2))$
Circumferential hydride fraction (-)	$0.067/2(1 + \exp(-(y - (h/2)^2)/(2(h/2)^2))$ $(1 - \cos(\pi * (x - r_i)/(r_o - r_i)))$

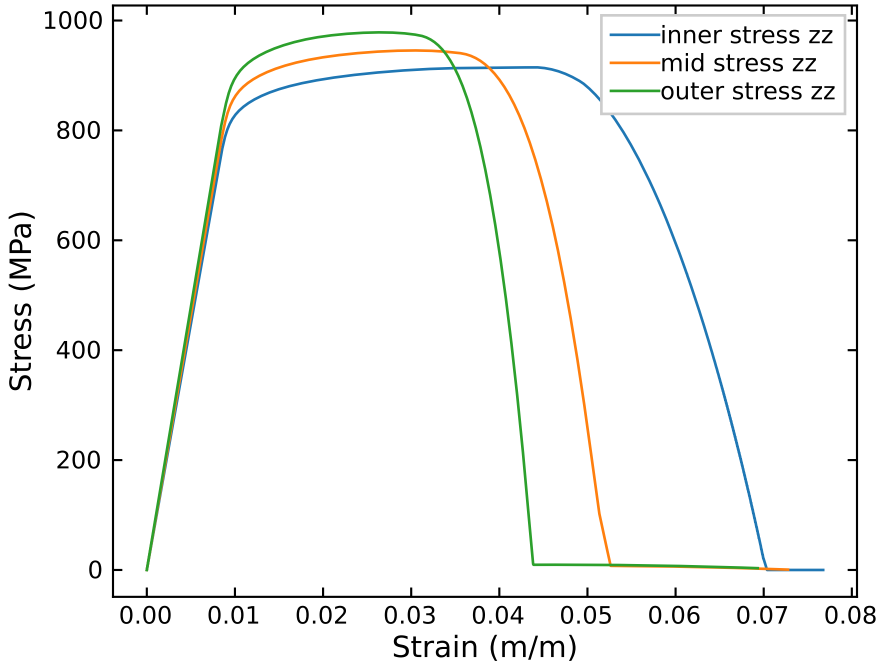

Figure 3.4. Evolution of stress for three locations in a slice of cladding with increasing radial displacement at the inner surface. Elastic, plastic, and damage stages are evident.

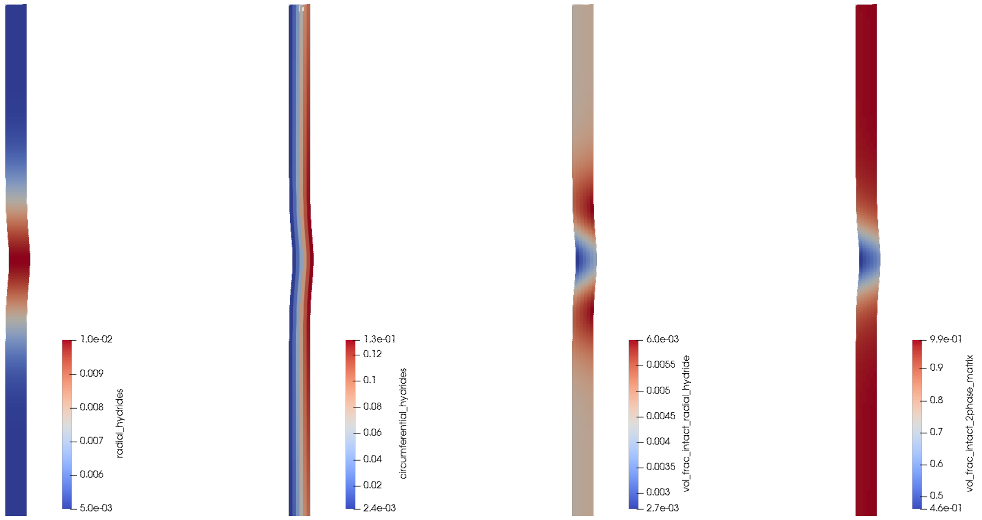

(a) Starting volume fraction of radial hydrides.

(b) Starting volume fraction of circumferential hydrides.

(c) Final volume fraction of intact radial hydrides.

(d) Final volume fraction of intact 2-phase matrix (Zircaloy plus circumferential hydrides).

Figure 3.5. Various volume fractions for a cladding tube pressurized to failure. Displacements magnified 10×.

Figure 3.6 shows the final hoop strain at the mid-height of the rodlet. The strain is greatest at the inner surface, in agreement with the volume fractions in Figure 3.5c and Figure 3.5d.

At the final state, the rodlet still shows a significant portion of undamaged material at mid-height. However, the stress at the inner surface at mid-height has reached its peak, as seen in Figure 3.7. The hoop strain at the same location is growing extremely quickly, indicating that the finite element model is unstable and burst has been reached.

This analysis demonstrates that the cladding damage model incorporates the effect of hydrides on the overall structural response of typical LWR cladding. The model includes a set of parameters that may be adjusted to best fit the elastic, plastic, and damage characteristics of the components of the cladding. Given this evidence and these characteristics, the model has the potential to be a useful tool in cladding burst calculations. However, the model needs adjustments to see broad use.

3.2.4 Future Work

As currently configured, the model is most useful for predicting burst in low temperature tubes. The calibration of critical parameters and validation can occur for these conditions once a corresponding set of experimental data is identified. Rashid et al. [6] give examples based on this type of data.

The cladding damage model is based on an elastic-plastic description of both the Zircaloy and the hydride. Creep is not considered. However, in high-temperature LOCA conditions, creep is an important mechanism

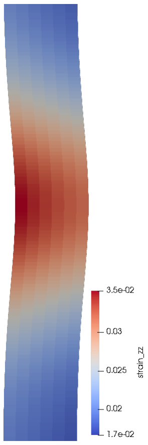

Figure 3.6. Final hoop strain in the rodlet at mid-height. The greatest strain is at the inner surface, which corresponds to the location of greatest damage.

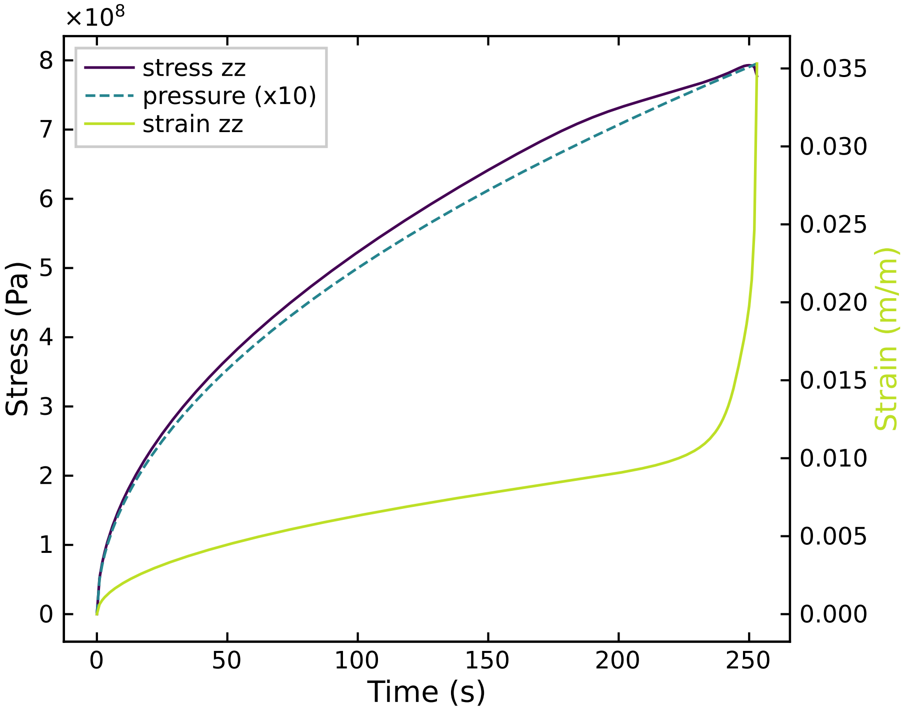

Figure 3.7. Evolution of hoop stress and strain at inner surface of rodlet at mid-height. The stress has begun to decrease at the end of the simulation. The strain is increasing dramatically. Applied pressure, scaled by a factor of 10, is also shown.

of cladding deformation.

The model as currently configured has the foundational ability to evolve damage based on the interaction of hydride platelets and Zircaloy and therefore shows merit for failure modeling of cladding tubes. It may be possible to reconfigure the model such that it accepts any constitutive law for either the Zicaloy or the hydride. If possible, this would allow creep in the Zircaloy while retaining the damage evolution characteristics of the model. Such an improvement would be needed for LOCA simulations and may also be of interest for spent fuel storage calculations. With such an enhancement, the model would be ready for calibration, benchmarking, and validation activities for a much wider set of conditions.

3.3 Anisotropic Zircaloy Creep

3.3.1 Implementation

An extension of inelastic mechanics capabilities was implemented and verified in Multiphysics Object-Oriented Simulation Environment (MOOSE). The inelastic deformation framework is based on a generalized return mapping that iterates on a scalar variable. A Hill's definition of the yield or compliance surface is employed. In other words, an equivalent stress measure is defined by

$$\sigma^2_{\Phi_{\text{Hill}}} = F(\sigma_{22}-\sigma_{33})^2 + G(\sigma_{33}-\sigma_{11})^2 + H(\sigma_{11}-\sigma_{22})^2 + 2L\sigma_{23}^2 + 2M\sigma_{31}^2 + 2N\sigma_{12}^2, \tag{3.8}$$

where F, G, H, L, M, and N are scalar coefficients that can be obtained experimentally to better capture the directional behavior of creeping and plastic materials. These coefficients are usually arranged in tensor form, as follows

$$\boldsymbol{A} = \begin{bmatrix} G+H & -H & -G & 0 & 0 & 0 \\ -H & F+H & -F & 0 & 0 & 0 \\ -G & -F & F+G & 0 & 0 & 0 \\ 0 & 0 & 0 & 2N & 0 & 0 \\ 0 & 0 & 0 & 0 & 2L & 0 \\ 0 & 0 & 0 & 0 & 0 & 2M \end{bmatrix}, \tag{3.9}$$

where $\boldsymbol{A}$ is usually referred to as Hill's tensor. This tensor representation as a function of anisotropic coefficients assumes the material is aligned with global axes. Using Eq. 3.9, one can define anisotropic creep compliance and anisotropic plastic yield surfaces [8, 9, 10]. Within the report [11], the following activities were carried out:

- **Generalized return mapping framework**. A hierarchy of classes to handle the return mapping for anisotropic materials was designed and created. This hierarchy is similar to the pre-existing isotropic one, since iterations occur on a single variable. However, the new hierarchy offers flexibility when passing deviatoric and full Cauchy stress tensors and enables simplification of the return mapping fallback options.

- **Hill's creep**. A Hill-like [8] yield function for creep was implemented in conjunction with a temperature-dependent power law (class name: `ADHillCreepStressUpdate`). This class has been expanded to address the more accurate physical approaches available in Bison in order to include, for example, thermal or irradiation dose dependencies.

- **Hill's plasticity**. Hill's plasticity with isotropic elastic behavior was implemented in the class `ADHillPlasticityStressUpdate`. Initial verification was performed.

- **Transformation of Hill's tensor and temperature-dependency**. The directional features of anisotropy are defined by the Hill's tensor. The implementation allows for defining temperature (texture) dependent anisotropy characteristics. In addition, rotation due to large deformation kinematics is included, which enables accurate simulation of cases such as ballooning in LOCA.

- **Creep numerical integration error.** The influence of the time step on the accuracy of the creep solution was investigated. An additional time step criterion, which is a function of the material point's stress increment, was added as an option to the user.

- **Application in Bison.** The inelastic implementation has been applied to a number of LOCA simulation scenarios in Bison in conjunction with advanced creep models. Further investigation is needed to better use experimental data capturing material's anisotropy.

4. Engineering-Scale Validation

The assessment and validation suite for LOCA analyses in Bison has been built up over the years. This year, no new cases have been added; however, a revisit of multiple integral and separate effects experiments has been completed utilizing the newly added pulverization thresholds and anisotropic creep capabilities as appropriate.

Recall that the hydrogen/hydride embrittlement and damage model is currently a plasticity-based model. During LOCA transients, the significant cladding distention experienced is driven by high-temperature thermal creep, and therefore at this time, the damage model is not included in the validation cases. See Section 3.2 for details on the model implementation, its testing in its current state, and the identification of future work to incorporate the hydrogen/hydride embrittlement and damage model LOCA analyses.

The test series revisited in this work include the Halden IFA-650 tests [12], the Studsvik 191 and 196 rods [13, 14], and the PUZRY [15] and REBEKA [16, 17, 18] cladding only burst tests.

The new anisotropic creep model is applied to the following cases: IFA-650.2, PUZRY, and REBEKA. The two lower length-scale pulverization thresholds are studied in Studsvik Rods 191 and 196 as well as IFA-650.4 and IFA-650.9. When using anisotropy of the cladding, the simulations consider the evolution of anisotropy for the two phases of Zircaloy-4. The model uses $F = 0.738$, $G = 0.588$, and $H = 0.174$ at room temperature and $F = 0.570$, $G = 0.480$, and $H = 0.450$ at 1073 K[a] [19]. Since no calibration of parameters was performed in this work (the anisotropic coefficients are taken from the literature for given thermally treated Zircaloy-4) and the originally isotropic Erbacher-Limback-Hoppe creep model is here numerically modified to account for creep anisotropy, the results presented in this section do not represent any form of validation but instead a measure of the influence of creep anisotropy on various LOCA modeling scenarios.

4.1 Halden IFA-650 LOCA Test Series

In total, 15 tests have been completed as part of the IFA-650 LOCA test series. Each test was designed for investigating a specific behavior by varying operational conditions, preirradiation history, plenum size, and cladding type, thus exploring the impact of these various phenomena on the behavior of the fuel rod during a LOCA. Of the 15 experiments completed, Rods IFA-650.2, IFA-650.4, IFA-650.9, and IFA-650.10 have been

---

[a] Note that due to the axisymmetric variable convention in MOOSE/Bison, and the orientation of the pins in the global frame, the order of these constants are modified in the input file (G and H values need to be swapped).

analyzed using Bison. The selection of these tests was primarily driven by the Bison team's participation in the Fuel Modelling in Accident Conditions (FUMAC) project [20]. The fabrication characteristics of the IFA-650.2, IFA-650.4, and IFA-650.9 specimens are provided in Table 4.1. IFA-650.10 is omitted from the table as this case has not been revisited in this work.

Table 4.1. Design data of the IFA-650.2, IFA-650.4, IFA-650.9 fuel rods [21, 22, 23].

	IFA-650.2	IFA-650.4	IFA-650.9
Fuel material	UO_2	UO_2	UO_2
Fuel density (%TD)	95.0	95.2	95.2
^{235}U enrichment (wt%)	2.0	3.5	3.25
Active fuel stack length (mm)	500	480	480
Pellet outer diameter (mm)	8.29	9.13	9.13
Cladding material	Zry-4	Zry-4	Zry-4
Cladding thickness (incl. liner[1]) (mm)	0.57	0.725	0.725
Cladding outer diameter (mm)	9.5	10.75	10.75
Diametral gap (μm)	70	170	170
Rod inner free volume (refab.) (cm^3)	17.4	21.5	19
Rod filling gas (refab.)	He	Ar(95%):He(5%)	Ar(95%):He(5%)
Initial rod inner pressure (refab.) (MPa)	4.0	4.0	4.0

[1] if present;

[2] For consistency with the fuel-cladding diametral gap width [24]

Details of the Halden IFA-650 tests are well documented [21, 22, 23, 24]. Each transient consists of five distinct phases: (1) preparatory (forced and natural circulation), (2) blowdown, (3) heat-up and hold at peak cladding temperature, (4) scram, and (5) conclusion of the experiment. The duration and specific conditions the specimen undergoes during a phase differs depending upon the specific experiment. The reader is encouraged to examine the appropriate documentation for a particular analysis if interested in more specific detail.

For all IFA-650 analyses presented here, the failure criterion used to determine cladding rupture and subsequent termination of the simulation is the plastic instability criterion. This criterion determines that the cladding is failed when the creep rate exceeds a value of 2.778×10^{-2} s^{-1} [25].

4.1.1 IFA-650.2

The second Halden LOCA test, IFA-650.2 [21], was performed in 2004 and consisted of a trial test using a fresh pressurized-water reactor (PWR) rod. The heat-up phase began 30–40 s after blowdown. Cladding burst failure occurred ~98.5 s after blowdown. Measured rod inner pressure at burst was ~5.6 MPa, and measured cladding temperature at burst was ~1080–1090 K. A 2D axisymmetric Bison model of the IFA-650.2 rod was constructed, following the design specifications from [21] (Table 4.1). The fuel pellet column was represented with a smeared fuel column. A single rod upper plenum was considered, with a volume corresponding to the total free volume in the more complex actual experiment [21].

In revisiting IFA-650.2, the primary interest is to evaluate the impact of including anisotropy in the creep behavior during the transient and how it affects the cladding profilometry predictions at the time of burst. The results are provided in Figure 4.1. While it can be seen that the magnitude of the outer diameter is similar, the location of the peak is shifted to be more in line with the location of the burst due to the inclusion of anisotropy. The influence of anisotropy appears to be far less than that of the failure criteria chosen as seen in [26].

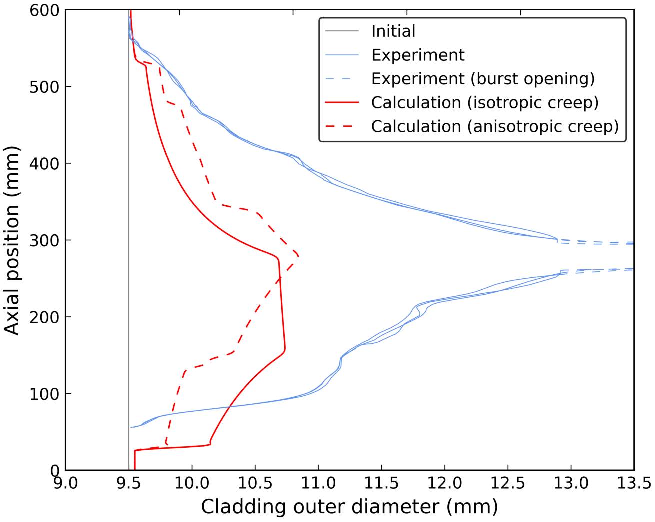

Figure 4.1. Comparisons of the cladding diameter at the time of burst between the Bison isotropic and anisotropic predictions and the experimental profilometry.

4.1.2 IFA-650.4

The IFA-650.4 test was the fourth test completed as part of the LOCA test series. The purpose of the test was to repeat the conditions of the IFA-650.3 test on a preirradiated fuel rod to assess the validity of existing LOCA safety criteria [22]. In particular, the experiment was designed in such a way to maximize the balloon size to promote fuel relocation and assess the impacts on cladding temperature and oxidation. The average burnup of the fuel after the base irradiation was $\sim 92\,\mathrm{MWd/kgU}$.

Due to the high burnup of the preirradiated fuel, severe fragmentation and axial relocation were observed during the transient. A large cladding balloon was also observed through gamma scans after the conclusion of the experiment. The maximum measured internal pressure was ~7.1 MPa achieved around 265–270 seconds after blowdown occurred. Cladding rupture occurred at ~366 s after blowdown.

Since the analysis uses the Bison axial relocation model to track fuel movement, the geometric representation of the rod is Layered1D, which simulates multiple radial slices individually while properly accounting for global parameters (i.e., rod internal pressure, fission gas release, rod internal volume). 30 axial layers were used to model the fuel and cladding with one additional cladding only layer for the plenum region. Eleven `EDGE3` elements were used through the radius of the fuel and five `EDGE3` elements were used through the cladding thickness. The base irradiation for IFA-650.4 is provided in Figure 4.2.

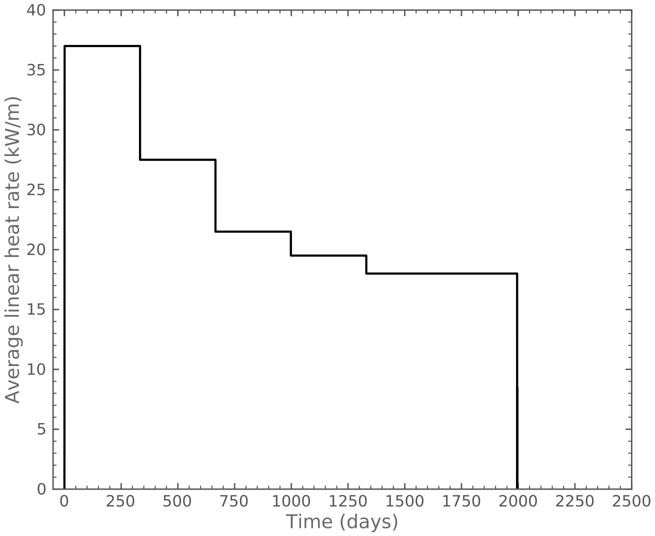

Figure 4.2. Base irradiation history for IFA-650.4

The primary interest in revisiting IFA-650.4 was to compare the differences in mass fraction axially throughout the rodlet due to the selection of the pulverization criteria. The pulverization criteria determines how much fuel is in small fragments, which is then used in the axial fuel relocation model to determine how the fuel moves throughout the rod. The amount of finely fragmented fuel is a crucial component to the axial relocation algorithm. The mass fraction predictions when using the three different pulverization thresholds are shown in Figure 4.3 alongside the experimental Cs-137 gamma scan taken 6 weeks after the conclusion of the experiment. The time to burst of each pulverization threshold is also important in explaining the behavior observed in Figure 4.3. These failure times are $\sim$ 316 s, $\sim$ 318 s, and $\sim$ 308 s for the empirical, analytical, and phase-field thresholds, respectively. The increased pulverization observed by the phase-field pulverization model results in improved packing of the fragments earlier in the transient for the large single balloon, leading to higher temperatures and higher creep rates at the location of distention causing the failure threshold to be reached at an earlier time.

4.1.3 IFA-650.9

The IFA-650.9 test was the ninth test completed as part of the LOCA test series. The purpose of this test was similar to IFA-650.4 and was used to clarify and confirm the behavior of significant fuel relocation that was observed in the previous test. The burnup of the fuel after the base irradiation was $\sim$89.9 MWd/kgU. Cladding ballooning began $\sim$106 s after blowdown at a maximum pressure of $\sim$7.33 MPa, and failure of the

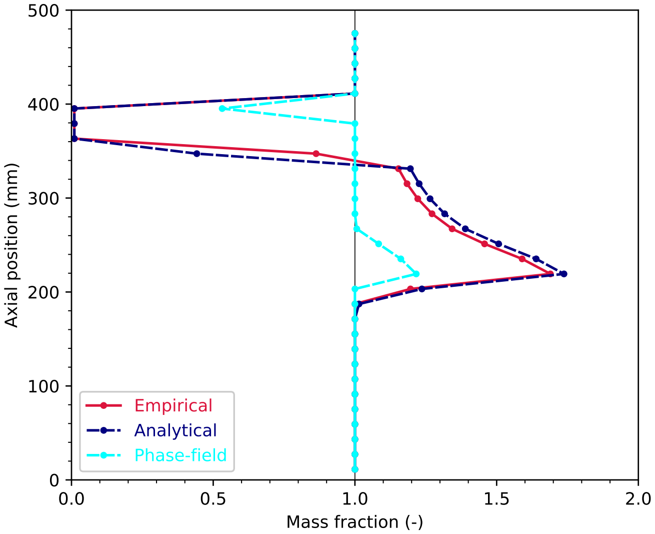

Figure 4.3. Mass relocation predictions for the empirical, analytical, and phase-field pulverization thresholds for IFA-650.4. The Cs-137 gamma scan is reproduced from [22].

cladding occurred at ∼133 s after blowdown at a cladding temperature of ∼1083 K.

The Layered1D formulation was also used for this rodlet. The same number of axial slices and mesh density as for IFA-650.4 were used. The base irradiation of this rod is provided in Figure 4.4.

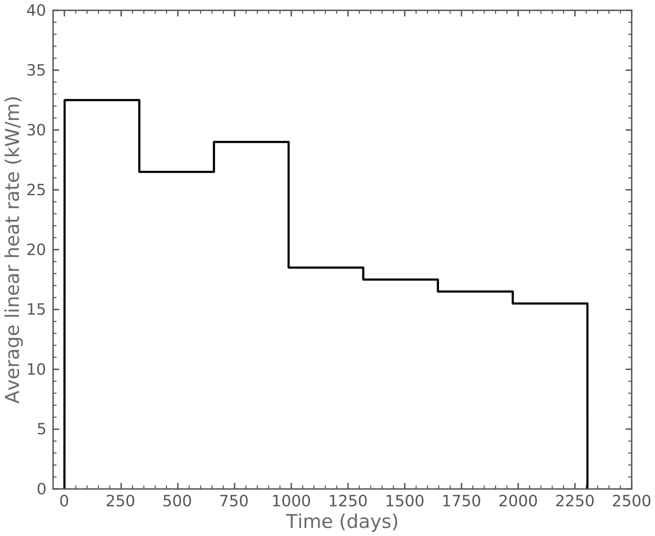

Figure 4.4. Base irradiation history for IFA-650.9

As with IFA-650.4, the result that could be influenced by the selection of the pulverization threshold is the mass relocation throughout the rodlet. The mass fraction predictions when using the three different pulverization thresholds are shown in Figure 4.5 alongside the experimental Cs-137 gamma scan. Contrarily to IFA-650.4, the phase-field pulverization threshold led to a cladding failure at a later time than the analytical model. Cladding failure times occurred at ∼139 s, ∼135 s, and ∼139 s, for empirical, analytical, and phase-field pulverization thresholds, respectively. The difference in model behavior compared to IFA-650.4 may be attributed to the fact that the cladding distention occurs in two balloons, which could affect the fuel relocation as a function of the quantity of pulverized fuel. Further work is necessary to understand this difference.

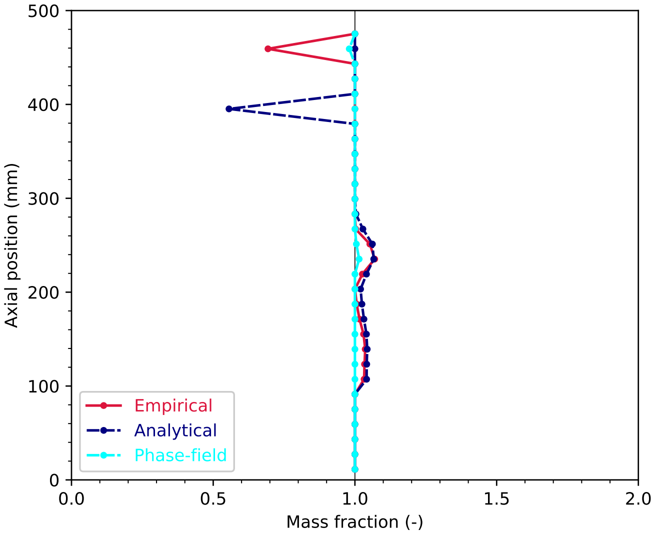

Figure 4.5. Mass relocation predictions for the empirical, analytical, and phase-field pulverization thresholds for IFA-650.9. The Cs-137 gamma scan is reproduced from [23].

4.2 Studsvik Rods 191 and 196

Bison contains models for two of the experiments conducted by the U.S. Nuclear Regulatory Commission (NRC) at Studsvik in Sweden [13, 27]. Rods 191 and 196 were chosen because Rod 191 experienced severe fine fragmentation while Rod 196 did not.

Information regarding the experimental conditions and pre-irradiation histories of Rods 191 and 196 have been obtained through publicly available documents [13, 27] and informed estimation when data is not available. Figure 4.6a illustrates the power history used to achieve the desired burnups prior to refabrication for the experiments. For Rod 191, this information was provided by EPRI and was said to be publicly known. For Rod 196, it is known that two cycles were used to achieve the discharge burnup (∼55 MWd/kgU) but that the detailed history is not available. Therefore, a representative two cycle irradiation was assumed.

After the base irradiation, the rodlets were refabricated and inserted into the Studsvik test train inside

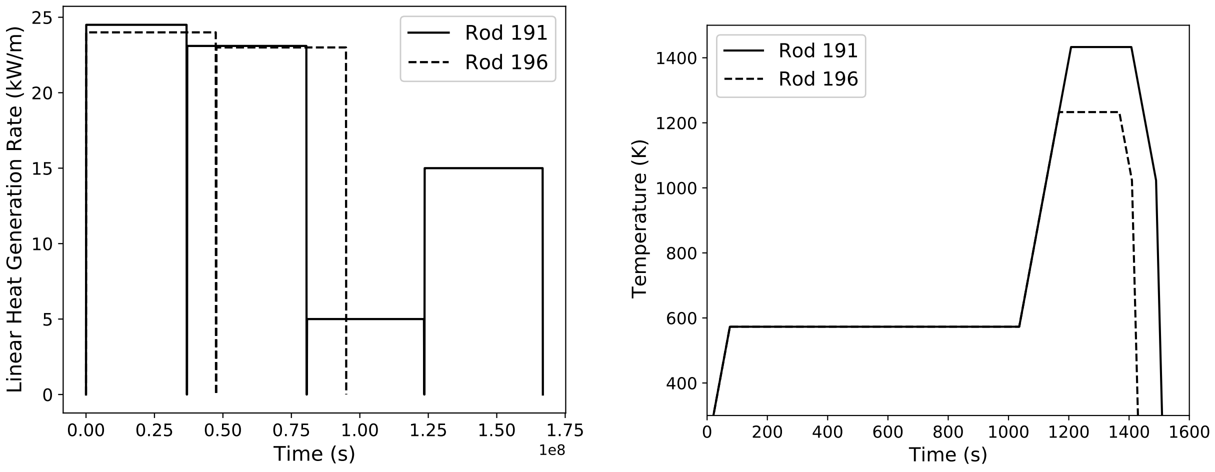

(a)

(b)

Figure 4.6. (a) The linear heat generation rate supplied to the rods during base irradiation and (b) the temperature applied to the cladding outer surface during the experiment.

a hot cell. The experimental specimens are subjected to external heating at a rate of 5°C/s to the target peak cladding temperature. This temperature was 1160°C and 960°C for Rods 191 and 196, respectively. Figure 4.6b illustrates the time history of the maximum temperature supplied to the cladding outer surface. This maximum occurs at the rod axial midplane. A slight axial profile on the temperature (20 K less at the ends) is assumed to induce localized ballooning. Table 4.2 provides additional information related to the two rods that is necessary for analysis. The additional free volume corresponds to the volume outside of the rod but able to communicate directly with the plenum (i.e., the pressure lines).

Table 4.2. Manufacturing and operational characteristics of Studsvik Rods 191 and 196 [13, 27].

	Rod 191	Rod 196
Rod height (mm)	300	300
Pellet stack height (mm)	265.4	260.6
Pellet radius (mm)	4.1	3.92
Gap thickness (mm)	0.08	0.08
Cladding thickness (mm)	0.57	0.57
Cladding material	. ZIRLO	ZIRLO
Upper plenum height (mm)	22.9	24.86
Lower plenum height (mm)	12.75	14.5
Fill gas (mm)	He	He
Fill gas pressure (MPa)	2 MPa	2 MPa
Refabrication pressure (MPa)	11 MPa	8.2 MPa
IFBA coating	NO	YES

A 2D-RZ axisymmetric representation was used to simulate the rods using information provided in

Table 4.2. For the thermal-hydraulic boundary condition during the base irradiation, the internal coolant channel model is used with an inlet pressure of 15.5 MPa, mass flow rate of 3800 kg/m^2-s, and an inlet temperature of 580 K. Many quantities of interest are tabulated by [13] for both rods, including balloon characteristics and the amount of fuel that was released during the transient. In the Bison simulations, it is assumed that all fuel that has exceeded the fine fragmentation threshold has been released from the rod. Table 4.3 provides a comparison between the Bison simulations for using the empirical Turnbull model [4] as well as the two lower length-scale-informed models, analytical and phase-field, alongside the experimental measurements for the total amount of fuel released during the LOCA. For both rods, the analytical model predicts zero fragmentation, while the phase-field fracture-based model overpredicts fragmentation relative to the empirical model. This overprediction is likely due to the fact that the model relies on an estimate of the initial HBS bubble pressure based on a dislocation punching criterion at the time of HBS formation, whereas in reality overpressurized bubbles are expected to grow after formation, decreasing their pressure. This decrease in initial pressure would lead to a smaller amount of pulverization when a transient occurs. The fact that the empirical model predicts some fuel release despite the average burnup of a lowered Rod 196 may be attributed to the assumption that all finely fragmented fuel releases from the rod. In the case of a lower average burnup, there may still be a pulverized portion in the pellet periphery, but the average particle size is larger than the opening of the cladding breach.

Table 4.3. Fuel mass released during the LOCA.

Rod 191		Rod 196	
Model	Mass Released (g)	Model	Mass Released (g)
Empirical	18.6	Empirical	6.56
Analytical	0	Analytical	0
Phase-field	25.4	Phase-field	16.2
Experiment	> 41	Experiment	0

4.3 PUZRY Burst Tests

The PUZRY rod ballooning tests were performed to investigate the mechanical behaviour and strength of Zircaloy cladding tubes and to provide adequate data for model validation. In particular, the effects of temperature and pressurization rate on the deformation and the failure (burst) pressure were investigated.

Thirty-one short Zircaloy-4 tube samples were investigated in a resistance furnace providing isothermal conditions in the temperature range of 700–1200°C. After an approximately 1000 s heat-up period, the sample was pressurized with Ar gas at a constant pressurization rate. Different pressurization rates between 0.005–0.263 bar/s were studied. The specimens were 50-mm-long pieces of Zircaloy-4 claddings with inner and outer diameters of 9.3 and 10.75 mm, respectively [15].

Two-dimensional axisymmetric models of the cladding tubes were created in Bison. The presence of the end plugs was accounted for by applying zero radial displacement boundary conditions to the tube surfaces in correspondence of the plugs. The furnace heating was simulated by a temperature boundary condition applied to the tube outer wall and consistent with the experimental conditions. A slight, linear variation of the temperature along the tube length was considered, with the total temperature difference being 6°C. The maximum temperature was considered at the tube mid-plane, which is consistent with visual inspections of the tested specimens showing ballooning around the mid-plane [15]. Taking advantage of the axial symmetry of the problem, only the lower half of the heated cladding length was modeled. Cases using the isotropic and anisotropic cladding creep models were simulated. It was found that the anisotropic creep algorithm had significant difficulty converging for the PUZRY cases. It is suspected that this is due to the type of loading condition, where the temperature is held constant and the pressure is linearly increased. The results are also highly dependent upon the selection of the `max_inelastic_increment` in the creep model, which limits the amount of creep that can occur in any given timestep. If one considers the REBEKA cases (see Section 4.4), there were no convergence issues. In those analyses, the loading condition was temperature driven rather than pressure driven.

Therefore, at this time, the results for calculated time to burst and rod internal pressure at burst are compared to the experimental data for a select set of fuel rods from the 31 completed as part of the PUZRY test series. Results are in Figures 4.7a and 4.7b. The rods selected, based upon their selection in the FUMAC project, are 10, 12, 18, 26, and 30. At low burst pressures, the differences between using anisotropic and isotropic creep of the cladding is minimal. However, as the burst pressure increases and the temperature of the specimens decreases, there is a visible improvement in comparisons when anistropy is included.

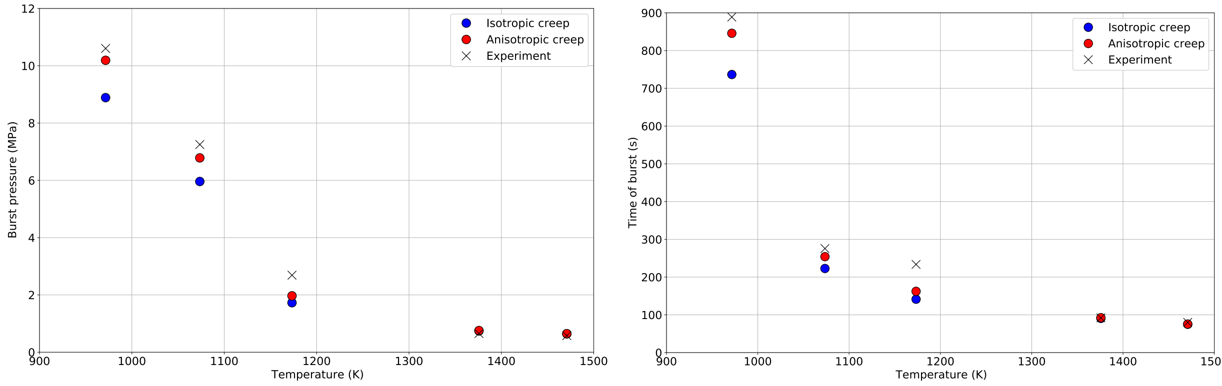

(a) (b)

Figure 4.7. (a) Pressure at burst and (b) time at burst as a function of specimen temperature. The pressure ramping rates were different for each case. (See [15])

4.4 REBEKA Burst Tests

The REBEKA separate effects tests [16, 17, 18] are temperature transient tests in steam performed on single PWR-size Zircaloy-4 tubes at a variety of internal pressures and heating rates. The purpose of the tests was to establish data of cladding ballooning and burst with reference to LOCA conditions. The cladding tubes had a fabricated inner and outer diameter of 9.30 and 10.75 mm, respectively, with a 325-mm heated length. The cladding was heated indirectly by conduction heating from inside using an electrically insulated heater rod. The test parameters covered a range of 1 to 14 MPa for the internal rod (He) pressure and 1 to 30 K/s for the heating rate. The test atmosphere was almost stagnant steam at atmospheric pressure and 473 K. The cladding temperatures were measured by thermocouples spot-welded on the outer surface of the cladding. More details on the experimental apparatus and conditions are given in [16, 17, 18]. In this work, only the rods with 1 K/s heating rates were considered.

Two-dimensional axisymmetric models of the cladding tubes were generated. The internal electric heating was simulated by a time-dependent Dirichlet temperature boundary condition applied to the tube inner wall and consistent with the experimental conditions. Pressure equal to the experimental value was applied at the tube inner wall. Taking advantage of the symmetry of the problem, only the lower half of the heated cladding length was modeled.

The Bison predictions are compared to the experiments for the burst temperature as a function of internal overpressure in Figure 4.8. Both the traditional isotropic and the new anisotropic models for cladding behavior were analyzed. At lower internal overpressures, both the isotropic and anisotropic models yield the same results. At higher pressures, the anisotropic model provides a slight improvement in the comparison to the experimental data.

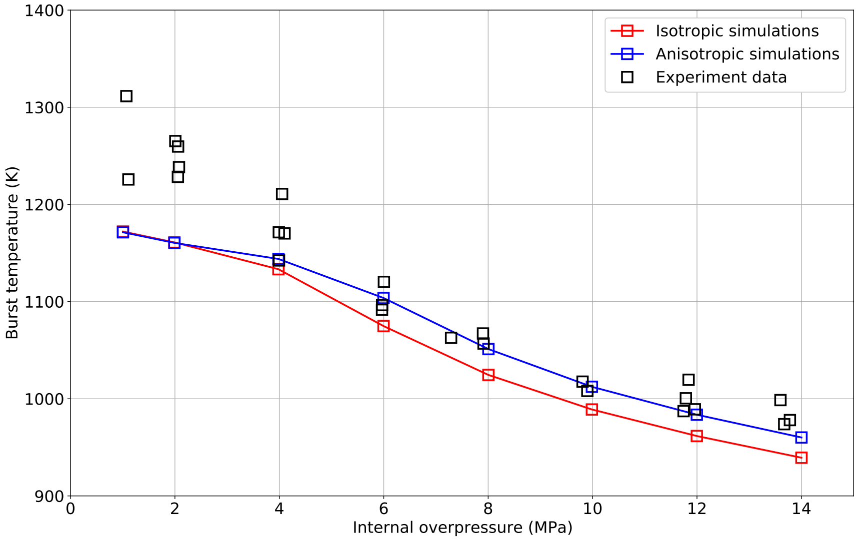

Figure 4.8. Comparisons of Bison simulations to experimental data of the 1 K/s REBEKA transients for both isotropic and anisotropic treatment of creep of the cladding.

5. Industry Relevant Problems

The nuclear industry is actively developing a technical basis to support extending the peak rod average burnup from 62 GWd/tU to ∼75 GWd/tU. However, high-burnup fuel FFRD has been identified as a safety issue that must be addressed prior to extending burnup. To address this safety concern, the nuclear industry is pursuing two parallel licensing approaches: 1) risk-informed and 2) fuel dispersal consequence analysis. The risk-based approach will develop a generic bounding analysis to exclude a large break loss-of-coolant accident (LB LOCA) as a safety concern, and thereby FFRD from licensing consideration. However, this approach would not exclude intermediate break (IB) and small break (SB) LOCAs from consideration. The IB and SB LOCA scenarios are intended to show cladding failure is precluded, mitigating the occurrence of FFRD. Fuel dispersal and consequence analysis on the other hand assumes FFRD occurs and will likely require the use of best-estimate tools to calculate fuel rod failure, pulverized UO_2 mass, fuel dispersal, and consequences of dispersal (i.e., criticality, dose, and coolability). Both approaches have their merits; however, each approach will likely require the use of a fuel performance code to inform the safety case by assessing high-burnup fuel performance. Furthermore, a successful safety case may hinge on the use of both approaches to disposition FFRD as a safety concern. Historically, safety cases have not used fuel performance codes to address a complex phenomenon like FFRD, and therefore, it is critical to assess fuel performance code capabilities.

NEAMS has taken an active role in developing modern methodologies for conservatively predicting FFRD. This role centers around assessing the state-of-the-art Bison fuel performance code capabilities for predicting FFRD with engineering-scale applications to inform the high-burnup safety case and evaluate those conditions where FFRD is a concern. Furthermore, the Bison results are being used to inform subsequent FFRD-related experiment and modeling research activates. The first objective was to evaluate the differences between electrically heated LOCA tests versus LOCA tests solely reliant on nuclear heating. A second objective is to inform the development of a no-burst criteria and a burst-opening model to inform UO_2 dispersal susceptibility.

The first objective was to identify differences, if any, between electrically heated LOCA tests and fully nuclear LOCA tests. Fuel pellet temperatures and stresses were calculated prior to an LOCA and during the transient, see Figure 5.1. Fuel temperatures reached minimum values with a completely flat profile at the end of the blowdown phase of the LOCA. Additional analyses addressed the possibility that immediate heating of the fuel rod might occur at the onset of the LOCA. Fuel temperatures from this hypothetical scenario were noticeably higher than those calculated with the blowdown included. However, the fuel stress profiles were effectively identical. These analyses concluded that the fuel pellet stress is governed by differential thermal expansion across the pellet relative to the pre-transient equilibrium state, and once the temperature profile becomes flat, the differential thermal expansion across the pellet does not change as the temperature uniformly increases. This has important implications because it suggests macroscopic stresses ∼27 seconds after the initiation of an LOCA test would be the same as those following a normal shutdown. Figure 5.2 compounds this conclusion as the stress profiles for fully nuclear results (blowdown) are identical to the electrically simulated LOCA test (no-blowdown) case. Linear heat rate (LHR) and burnup sensitivity studies were performed to determine the primary cause for macroscopic stress formation. LHR was shown to be directly correlated to the stresses induced during the blowdown phase of the LOCA, and burnup had no effect on fuel stresses. This behavior confirms that macroscopic fuel stresses generated during a LOCA are directly correlated to the pre-transient operating conditions (i.e., LHR), and it also confirms that LOCA heating conditions (e.g., decay heat or external heat) have no impact on the formation of macroscopic stresses.

The second objective assessed cladding performance during LOCA in an effort to inform the no-burst criteria. The analysis assessed the differences between the expected behavior of commercial fuel rods and cladding experiments under conditions where cladding burst rupture is expected to occur. Commercial fuel rod evaluations during LOCA suggested that commercial fuel rods will burst at higher temperatures than those observed in simulated LOCA tests. There are several possible reasons for this observed behavior. First, commercial fuel rods are significantly longer (∼3.6–3.9 m) than rodlets used in a simulated LOCA test (0.3 m). Because commercial fuel rods have a smaller fuel-to-volume ratio and a changing temperature profile, the rod internal pressure decreases at a faster rate as the cladding internal volume increases. This sustained pressure allows ballooning to occur axially along the cladding with the increased deformation corresponding to higher temperatures. Fuel rod temperatures uniformly increase until the reflood process begins, quenching the fuel rod from bottom to top. As the reflood process progresses, local axial regions of the fuel rod cool, thereby terminating the local ballooning process. This results in subsequently smaller changes to the fuel rod's internal volume and pressure conditions. Consequently, upper spans of the cladding tube are subject to increased temperatures for a longer period, allowing larger balloon sizes to form, increasing the likelihood of burst.

The final objective was to develop a burst-opening model to support dispersal susceptibility characterization. To date, modeling the burst opening has not been prioritized as there has not been cause to consider the burst size. However, burnup extension may require the nuclear industry to consider quantifying fuel dispersal. With fuel dispersal in mind, the shape and size of the rupture opening may be an important consideration as fuel fragments are required to be smaller than the rupture opening to physically disperse through the cladding rupture opening. Reference [28] indicated that the size of the burst opening was proportional to the amount of fuel dispersal and suggested large amounts of dispersal required the area of the burst opening to be greater than ∼80-100 mm^2. Therefore, quantifying the burst opening may allow minimization of fuel dispersal and its consequences.

This milestone documents an extensive literature search. This literature review evaluated cladding-burst

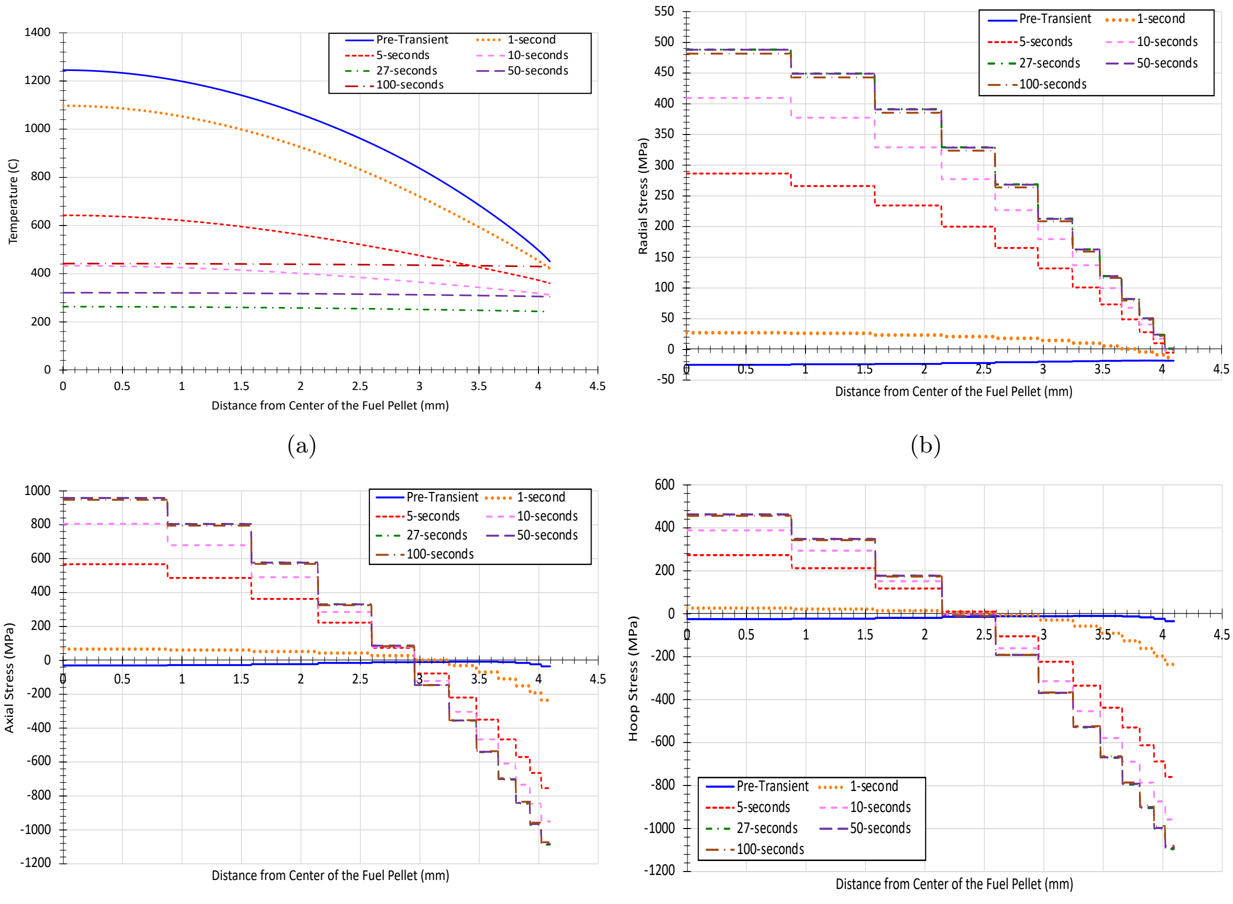

(a) (b)

(c) (d)

Figure 5.1. R-Z fuel response during a simulated LOCA transient: (a) radial temperature, (b) radial stress, (c) axial stress, and (d) hoop stress. Note the end of the blowdown phase and the start of the refill phase occurs at 27 seconds.

tests on different types of Zr-alloy tubes with varying tube geometries. The raw data were evaluated and compared against a number of different parameters, and through this comparison, it was determined that rupture opening closely tracked the balloon deformation.

Figure 5.3 compares the developed burst opening model (see ORNL/SPR-2021/2218 for model details) results to the experimental data. The figure highlights multiple assumed geometries, and the oval-shaped rupture geometry was determined to provide a conservative and realistic burst size. The burst area of most of the outliers is attributed to test rodlets that experienced a significant amount of rod bending during the test. The successful use of this model requires an accurate prediction of balloon geometry and, as indicated in the milestone report, the existing high-temperature cladding creep model needs to be improved for the burst model to provide impactful results.

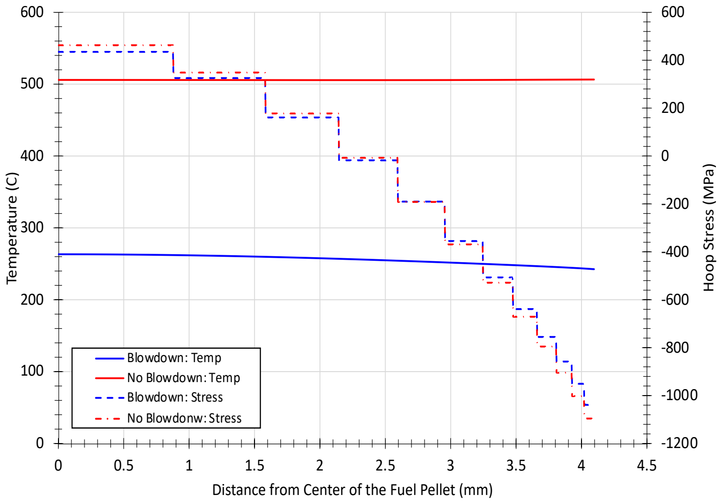

Figure 5.2. Comparison of the blowdown and no-blowdown fuel temperature and hoop stress profiles in R-Z space at 27 seconds after LOCA initiation.

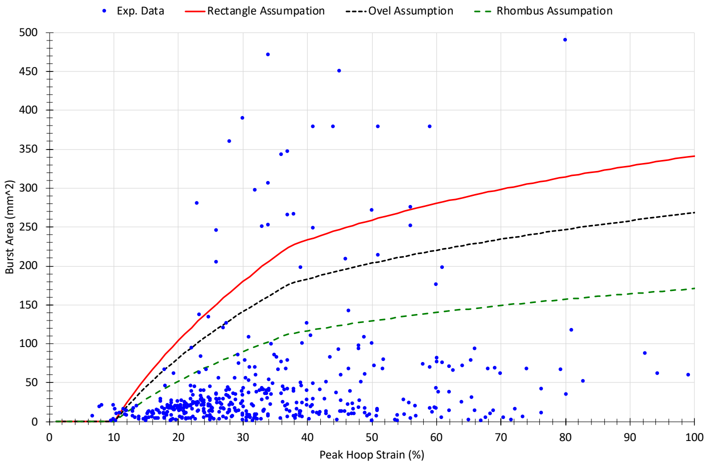

Figure 5.3. Comparison of cladding rupture area as a function of peak cladding hoop strain for available literature data and limiting model

The work performed in this milestone report highlighted a number of improvements needed to predict FFRD. Bison fuel stress analysis results indicate macroscopic fuel stresses were insufficient to stimulate pulverization. This points to a need for Bison to incorporate lower length-scale capabilities to better predict stresses that form as a result of microscopic features (i.e., fission gas bubbles, grain boundary degradation). The NEAMS program is currently using MARMOT coupled with atomistic modeling efforts (i.e., DFT, MD, and CD) to develop mechanistic models to fill the identified gaps and accurately predict UO_2 pulverization.

NEAMS report ORNL/SPR-2021/2218 Bison cladding results indicate the current high-temperature thermal creep was insufficient to accurately predict cladding ballooning and burst. Bison simulations have been shown to reach the burst temperature accurately; however, the cladding balloon strain is under-predicted. A mechanistic cladding high-temperature thermal creep model is currently under development to better capture the impact of microstructural changes on the cladding deformation. This model intends to leverage results from many lower-length scale simulations, distilling them into a simpler form for implementation in the fuel performance code. The model improvements are expected to enable more accurate simulations of the cladding under rupture conditions. Coupling these model improvements to in situ and high-fidelity cladding creep and burst data will also enhance Bison's ability to predict LOCA performance and burst opening, especially in commercial fuel rod applications.

6. AFC/NEAMS Collaboration

Historical integral LOCA tests leveraged infrared lamps to heat rodlets at a constant rate of 5°C/s [29, 28]. However, this may not be representative of in-reactor LOCA conditions. A collaboration between NEAMS and AFC was prioritized to assess data gaps between historical LOCA experiments and in-reactor performance and the ability for the TREAT and SATS facilities to address these gaps. In essence, the approach intends to identify and design a test matrix that leverages the throughput capabilities of SATS to identify high-impact tests in the TREAT facility. This approach requires a thorough understanding of both steady-state and transient high-burnup conditions. Furthermore, best-estimate and best-estimate-plus uncertainty considerations are required to develop a comprehensive operation envelop for high-burnup fuel.

TREAT reactor and SATS LOCA analyses were performed and compared to commercial fuel rod analyses. These analyses were performed using DOE tools to ensure planned LOCA tests are prototypical and consistent with industry experience. The culmination of this effort intends to support the development of an integral and semi-integral test matrix designed to successfully form the foundation of high burnup FFRD topical reports and inform the community on FFRD behavior.

LOCA thermal hydraulic modeling has been historically limited to the so-called “hot rod.” However, there are instances where high-burnup fuel rod conditions were also evaluated. These evaluations are summarized in Figure 6.1 where Figure 6.1a highlights the thermal hydraulic analysis results for a high-burnup fuel rod located in the center of the core (i.e., best estimate/red curve) and a hot rod (green curve) [30]. A bounding case (black curve) applied a 20% uncertainty to the hot rod scenario to generate a peak cladding temperature (PCT) similar to traditional integral LOCA tests. Figure 6.1b was a similar analysis that evaluated the hot rod cladding temperature for a core containing high-burnup fuel [31]. A point to note is that neither the burnup for the hot rod, nor the core design or location of the fuel rod are discussed. However, when comparing the end-of-cycle (EOC) result in Figure 6.1b to the hot rod result (green curve) in Figure 6.1a, the PCT notably similar. One difference between the two results is the general system response. Figure 6.1a has a much slower heating rate (∼3–5°C/s), whereas the heating rate in Figure 6.1b starts at ∼35–45°C/s before decreasing to 4–5°C/s near the expected burst temperature. These results indicate that LOCA heating rates may vary between reactor types as each system responds differently. Therefore, any integral LOCA testing would need to be able to handle a wide range of heating rates to appropriately represent prototypical LOCA conditions.

The results of this collaboration can be seen in Figure 6.2 and Figure 6.3. The severe accident test station

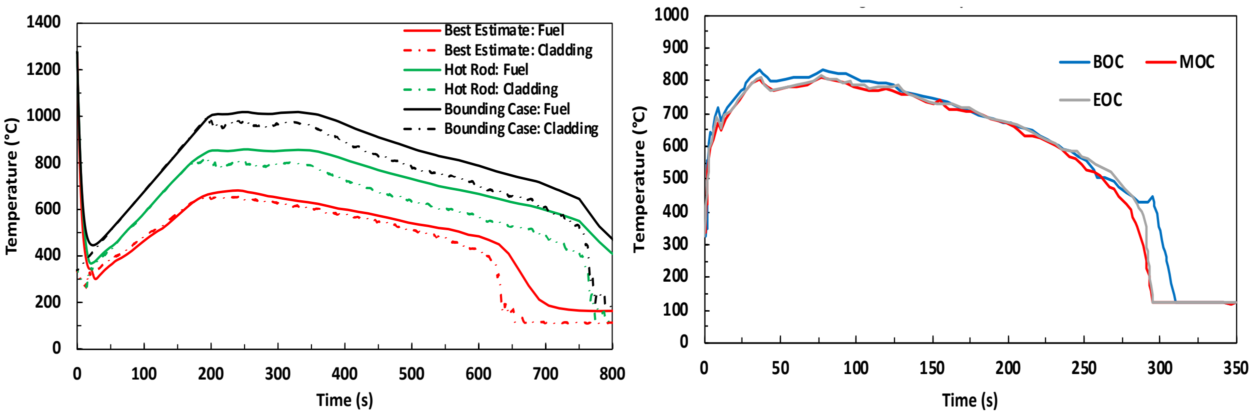

(a) (b)

Figure 6.1. (a) LOCA cladding temperature for best estimate high-burnup fuel rod, hot rod, and bounding case [30] and (b) hot rod scenario for a core containing high-burnup fuel [31].

(SATS) has the ability to simulate LOCA heating rates ranging from ∼1°C/s up to ∼20°C/s as well as to vary the heating rates during the heatup phase. One limitation of the SATS test is the inability to simulate the pre-transient nuclear conditions prior to the LOCA. The TREAT reactor is uniquely qualified to address these critical data. Figure 6.3 highlights the TREAT reactor's ability to experimentally simulate Westinghouse 4-loop PWR LOCA conditions calculated by TRACE (Figure 6.3a) and RELAP (Figure 6.3b) and expected in-reactor conditions. Additionally, the TREAT reactor can experimentally simulate historical infrared furnace LOCA heating tests (Figure 6.3c) to replicate SATS test conditions, allowing full demonstration of the differences between electrically heated and fully nuclear heated LOCA tests.

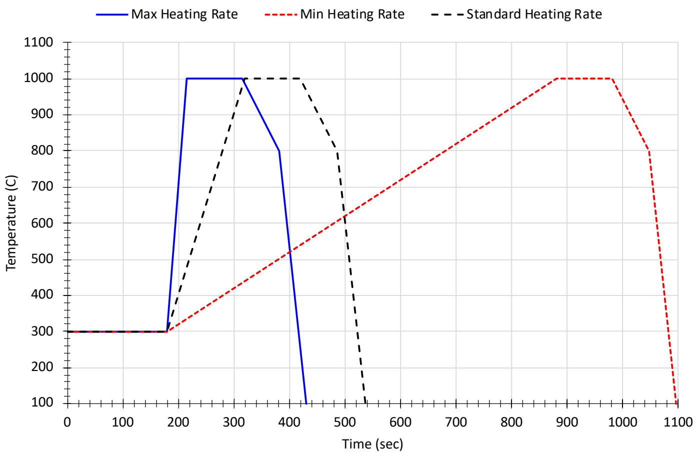

Figure 6.2. SATS semi-integral LOCA tests heating rate capabilities [29].

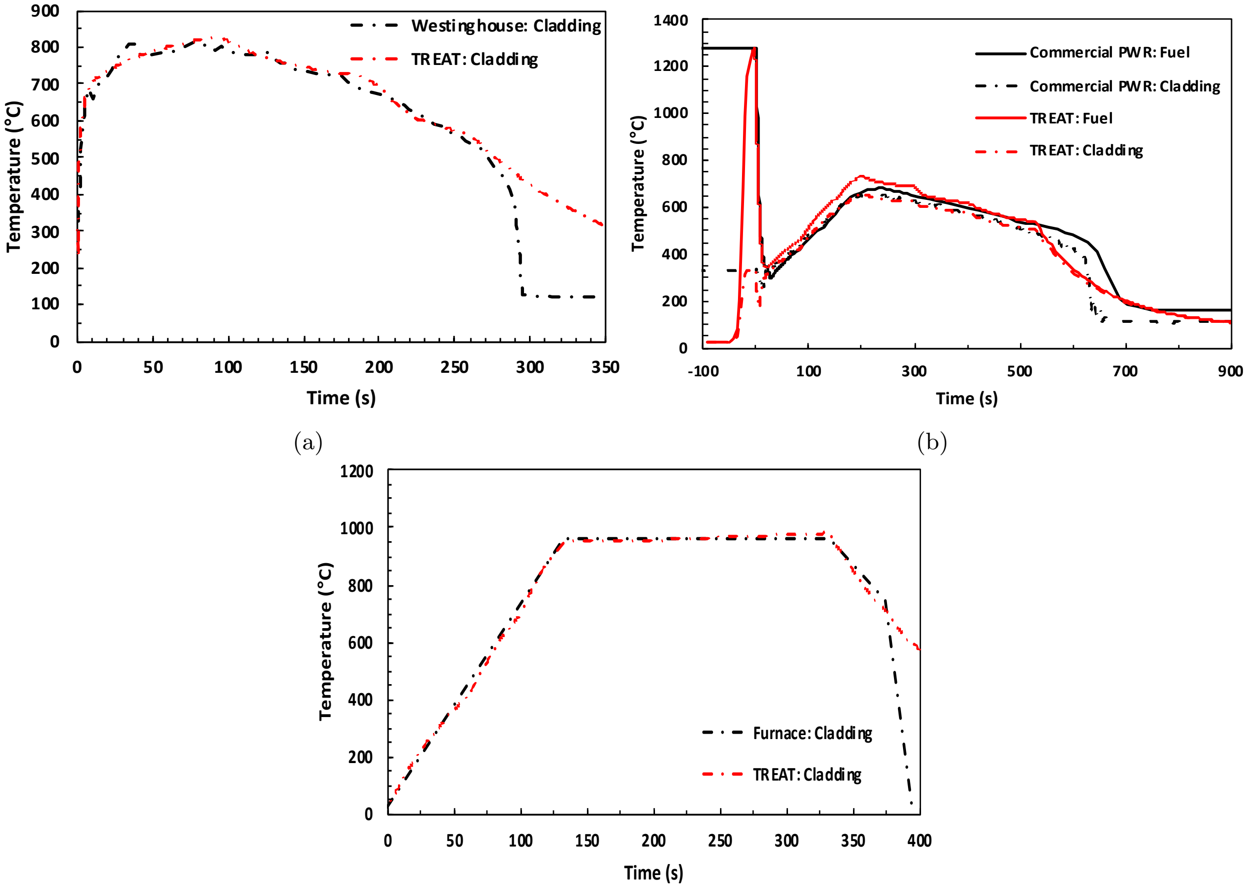

(a)

(b)

(c)

Figure 6.3. Analysis results demonstrating the TREAT reactor's ability to prototypically represent (a) TRACE Westinghouse 4-loop PWR, (b) RELAP5-3D Westinghouse 4-loop PWR, and (c) SATS furnace-style tests.

7. Conclusions

There are advancements in the modeling capabilities of Bison for LOCA transients. A multiscale modeling approach was developed to gain insight into the mechanisms driving fine fuel fragmentation. Cladding behavior models were added from the literature to more accurately capture fuel phenomena. These models were used in a handful of existing Bison validation cases to assess their impact on model predictions. The two lower length-scale pulverization models (analytical and phase-field) resulted in predictions that bounded the existing empirical Turnbull threshold [4]. The inclusion of anisotropic effects on the creep behavior of Zircaloy yielded improved predictions under high internal pressure-loading conditions and was more stable under temperature driven deformation. Limited impact was observed at lower pressure-loading conditions. For cases when temperature was held constant and the pressure was increased (i.e., PUZRY), the numerical stability of the analyses was greatly impacted. Note the major assumption made when implementing the preliminary anisotropic creep model for Zircaloy was to wrap the Hill coefficients algorithm around an originally isotropic creep correlation. This assumption could have influenced all of the results presented in the Section 4 of this report. The added hydrogen/hydride embrittlement and damage model was demonstrated to provide correct predictions for a variety of analytical test cases.

Bison was also applied to industry-relevant problems by investigating the stress state within the fuel prior to a LOCA and the impact the transient testing approach has on the evolution of the stress state during the transient. The testing approaches considered were electrically heated and nuclear-heated LOCA tests. A preliminary burst opening criteria was also developed.

Finally, an overview of the collaboration between the NEAMS and AFC programs was provided to highlight modeling and simulation use to identify experimental tests that can be executed in the AFC-funded experimental facilities, the TREAT facility and SATS.

8. Future work

While there has been progress in improving the understanding of the mechanisms of fuel fragmentation and extending cladding model capabilities to include hydrogen embrittlement, hydride damage, and anisotropic creep, there is more work to complete. Further developments in the area of FFRD and cladding behavior include:

- Continued refinement of the mesoscale-informed fuel pulverization threshold in Bison including 3D calculations of the HBS microstructure, improvements in the evolution of the gas bubble pressure during the transient, and analyses of partially recrystallized regions to find the threshold of recrystallization required for pulverization to occur.
- Extend the hydrogen/hydride embrittlement and damage model to work with other inelastic creep models (i.e., creep) since it is currently based only on plasticity. In addition, the mechanical properties of the hydride and matrix (i.e., Zircaloy) are currently input as constant properties. Ideally, the mechanical properties used in the embrittlement and damage model would be coupled directly to existing models in Bison that depend on temperature, neutron fluence, and manufacturing technique (e.g., stress-relief annealed and recrystallization-annealed dependence).
- The anisotropic creep model used in this work was supported by another NEAMS work package. It leverages the automatic differentiation system in MOOSE, which is not yet supported for generalized plane-strain analyses, which is what the Layered1D framework used in the IFA-650.4 and IFA-650.9 cases depends upon. In the future, the anisotropic creep model should be extended so it can be used in the Layered1D framework as it will impact the predictions of fuel movement in those analyses. The end goal for modeling the behavior of the cladding would be to use a reduced-order model formed from a complete Visco-Plasticity Self-Consistent (VPSC) model for the response of the cladding during a LOCA transient.
- Continued work is necessary on developing and implementing the cladding burst opening model into Bison.

Bibliography

[1] R. L. Williamson et al. "BISON: A Flexible Code for Advanced Simulation of the Performance of Multiple Nuclear Fuel Forms". In: *Nuclear Technology* 207.7 (2021), pp. 954–980. DOI: `10.1080/00295450.2020.1836940`.

[2] T. Sonoda. et al. "Transmission electron microscopy observation on irradiation-induced microstructural evolution in high burn-up UO_2 disk fuel". In: *Nuclear Instruments and Methods in Physics Research Section B: Beam Interactions with Materials and Atoms* 191 (2002), pp. 622–628.

[3] M. W. D. Cooper and D. A. Andersson. *Fuel Pulverization During Temperature Ramps: Molecular Dynamics Simulations.* Tech. rep. 3002020945. EPRI, 2021.

[4] J. A. Turnbull et al. "An Assessment of The Fuel Pulverization Threshold During LOCA-Type Temperature Transients". In: *Nuclear Science and Engineering* 179 (2015), pp. 477–485. DOI: `https://doi.org/10.13182/NSE14-20`.

[5] L. K. Aagesen et al. *Mesoscale simulations to inform microstructure-based pulverization criterion in high-burnup* UO_2. Tech. rep. INL/EXT-21-64275. Idaho National Laboratory, 2021.

[6] Joe Rashid et al. "A New Material Constitutive Model for Predicting Cladding Failure". In: *Proceedings of Top Fuel 2009.* Paris, France, 2009.

[7] G. P. Bazeley et al. "Triangular Elements in Plate Bending–Conforming and Nonconforming Solutions". In: *Proceedings of the Conference on Matrix Methods in Structural Mechanics.* Wright Patterson Air Force Base, Dayton, Ohio, 1965, pp. 547–576.

[8] R. Hill. *The Mathematical Theory of Plasticity.* Oxford engineering science series. Clarendon Press, 1950.

[9] C. M. Stewart et al. "An anisotropic tertiary creep damage constitutive model for anisotropic materials". In: *International Journal of Pressure Vessels and Piping* 88.8-9 (2011), pp. 356–364. DOI: `https://doi.org/10.1016/j.ijpvp.2011.06.010`.

[10] D. Versino and K. C. Bennett. "Generalized radial-return mapping algorithm for anisotropic von Mises plasticity framed in material eigenspace". In: *International Journal for Numerical Methods in Engineering* 116.3 (2018), pp. 202–222. DOI: `https://doi.org/10.1002/nme.5921`.

[11] Recuero A., Schwen D., and Biswas S. *M3 Milestone: Anisotropic Inelastic Deformation.* Tech. rep. INL/EXT-21-62011 Rev. 1. Idaho National Laboratory, 2021.

[12] T. Fuketa et al. *Safety Significance of the Halden IFA-650 LOCA Test Results.* Tech. rep. NEA/CSNI/R(2010)5. Organisation for Econocmi Co-operation and Development Nuclear Energy Agency Committee on thte Safety of Nuclear Installations, 2010.

[13] M. Flanagan and P. Askeljung. "Observations of Fuel Fragmentation, Mobility and Release in Integral High-Burnup, Fueled LOCA Tests". In: *Enlarged Halden Program Group Meeting 2011.* 2011.

[14] A. Puranen. *Post test examinations on LOCA tested rods.* Tech. rep. STUDSVIK/N-13/198. Studsvik, 2013.

[15] E. Perez-Feró et al. *Experimental Database of E110 Claddings under Accident Conditions.* Tech. rep. EK-FRL-2012-255-01/02. Budapest, Hungary: Centre for Energy Research, Hungarian Academy of Sciences, 2013.

[16] F. J. Erbacher et al. "Burst criterion of Zircaloy fuel claddings in a loss-of-coolant accident". In: *Zirconium in the Nuclear Industry, Fifth Conference, ASTM STP 754, D.G. Franklin Ed.* American Society for Testing and Materials. 1982, pp. 271–283.

[17] M. E. Markiewicz and F.J. Erbacher. *Experiments on ballooning in pressurized and transiently heated Zircaloy-4 tubes.* Tech. rep. KfK 4343. Kernforschungszentrum Karlsruhe, Germany: Kernforschungszentrum Karlsruhe GmbH (Germany, 1988.

[18] F.J. Erbacher, H.J. Neitzel, and K. Wiehr. Tech. rep. KfK 4781. Kernforschungszentrum, Karlsruhe, 1990.

[19] H. E. Rosinger, J. Bowden, and R. S. W. Shewfelt. *The anisotropic creep behaviour of Zircaloy-4 fuel cladding at 1073 K.* Tech. rep. AECL-6447. Pinawa, Manitoba, Whiteshell Nuclear Research Establishment: Atomic Energy of Canada Ltd., 1982.

[20] International Atomic Energy Agency. *Fuel Modeling in Accident Conditions (FUMAC) Final: Final Report of a Coordinated Research Project.* Tech. rep. IAEA-TECDOC-1889. International Atomic Energy Agency, 2019.

[21] M. Ek. *LOCA Testing at Halden; The Second Experiment IFA-650.2.* Tech. rep. HWR-813. OECD Halden Reactor Project, 2005.

[22] L. Kekkonen. *LOCA Testing at Halden; The Fourth Experiment IFA-650.4.* Tech. rep. HWR-838. OECD Halden Reactor Project, 2007.

[23] Bole du Chomont F. *LOCA Testing at Halden; The Ninth Experiment IFA-650.9.* Tech. rep. HWR-917. OECD Halden Reactor Project, 2009.

[24] A. Lavoil. *LOCA Testing at Halden; The Tenth Experiment IFA-650.10.* Tech. rep. HWR-974. OECD Halden Reactor Project, 2010.

[25] V. Di Marcello et al. “The TRANSURANUS mechanical model for large strain analysis”. In: *Nuclear Engineering and Design* 276 (2014), pp. 19–29. DOI: `https://doi.org/10.1016/j.nucengdes.2014.04.041`.

[26] G. Pastore et al. “Analysis of fuel rod behavior during loss-of-coolant accidents using the BISON code: Fuel modeling developments and simulation of integral experiments”. In: *Journal of Nuclear Materials* 545 (2021), p. 152645. DOI: `https://doi.org/10.1016/j.jnucmat.2020.152645`.

[27] M. Helin and J. Flygare. *NRC LOCA tests at Studsvik, Design and construction of test train device and tests with unirradiated cladding material*. Tech. rep. STUDSVIK/N-11/130. Studsvik, 2012.

[28] N. Capps et al. “A Critical Review of High Burnup Fuel Fragmentation, Relocation, and Dispersal under Loss-Of-Coolant Accident Conditions”. In: *Journal of Nuclear Materials* 546 (2021), p. 152750. DOI: `https://doi.org/10.1016/j.jnucmat.2020.152750`.

[29] N. Capps et al. “Integral LOCA fragmentation test on high-burnup fuel”. In: *Nuclear Engineering and Design* 367 (2020), p. 110811. DOI: `https://doi.org/10.1016/j.nucengdes.2020.110811`.

[30] N. Capps et al. “Full core LOCA safety for a PWR containing high burnup fuel”. In: *Nuclear Engineering and Design* under review (2020).

[31] P. Raynaud and I. Porter. “Predictions of fuel dispersal during a LOCA”. In: *Proceedings of WRFPM 2014*. Sendai, Japan, 2014.